



Interaction of quasi-two-dimensional vortical gusts with airfoils, unswept and swept wings

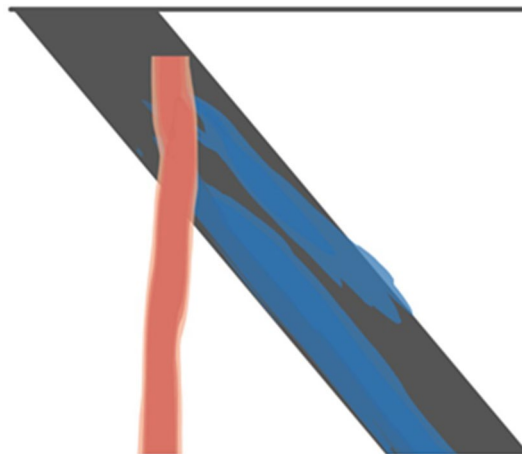
Yuanzhi Qian¹ · Zhijin Wang¹ · Ismet Gursul¹

Received: 19 April 2022 / Revised: 26 June 2022 / Accepted: 8 July 2022 / Published online: 3 August 2022
© The Author(s) 2022

Abstract

A nearly two-dimensional vortex of small core size has been produced by the transient plunging motion of an upstream airfoil and it interacted with the downstream wings. Depending on the offset distance of the vortex and wing angle of attack, the incident vortex filament deforms, diffuses, and loses coherence, while inducing leading-edge vortex formation and shedding from the wing. No significant spanwise flow develops in the incident vortices during the interaction. The interaction with the swept wing at each spanwise plane appears to be unaffected by the other spanwise planes. The counter-clockwise vortex induces a positive lift peak as it approaches the wing, which can be predicted by the potential flow assumption. The peak lift force is proportional to the circulation of the incident vortex and has its maximum near the zero-offset distance. The minimum lift coefficient is reached after the vortex has just passed and caused flow separation on the lower surface. The maximum lift coefficients for the finite unswept and swept wings can be estimated by making a correction for the aspect ratio and using the independence principle. The only exception is observed for the swept wing at a post-stall angle of attack for which the leading-edge vortex shedding becomes parallel to the leading-edge and increases the peak lift force.

Graphical abstract



1 Introduction

Gusts are often considered and simulated as vorticity concentrations (vortex filaments), although irrotational gusts are certainly a possibility. As vorticity-based representations and interpretations are preferred (Rockwell 1998), here we focus on vortical-gusts. Interaction of parallel, streamwise and normal vortices with downstream airfoils can be considered

✉ Ismet Gursul
i.a.gursul@bath.ac.uk

¹ University of Bath, Bath BA2 7AY, UK

to contain all the elementary aspects of the gust-wing interactions. Parallel vortex interactions are expected to have more significant influence on the aerodynamic forces, as the streamwise and normal vortices are likely to affect a small fraction of the wing-span. As the vortical structures become stronger and more concentrated, the interaction with airfoils becomes more challenging as the localized flow separation is likely to occur (Jones et al. 2022). Concentrated vortical gusts differ from other gusts for which the gust cross-stream length scale is large compared to the airfoil dimensions. The vortical gusts may be considered to represent more realistic gusts with large but localized velocity fluctuations.

Two-dimensional aspects of the interaction of gusts with airfoils are mostly understood. Parallel vortex-airfoil interactions were reviewed by Rockwell (1998). General features of the interaction include two main aspects: (i) distortion of the incident vortex, if the distance between the vortex and airfoil is small, and (ii) shedding of the secondary vortex of the opposite sign from the wing (Doligalski et al. 1994). The first effect is believed to be an essentially inviscid phenomenon (Rockwell 1998). The second effect relies on the generation of secondary vorticity, which is a viscous phenomenon. Subsequent roll-up of vorticity into coherent vortices was discussed by Rockwell (1998). The point-vortex models (Chen and Jaworski 2020) and the discrete-vortex models (Panaras 1987) capture the inviscid aspects of the vortex-airfoil interaction. Numerical simulations were able to capture the viscous interactions of close vortex-airfoil encounters, including the transition to turbulence in the leading-edge vortex and the boundary layers at transitional Reynolds numbers (Barnes & Visbal, 2018a, 2018b). It was found that, with increasing angle of attack and vortex core size, more intense viscous interactions result in the formation of leading-edge vortices (Barnes & Visbal 2020).

In experimental investigations, various vortex configurations were considered: a separated shear layer impinging on a corner (Rockwell and Knisely 1979); mixing layers of two streams interacting with sharp and elliptical leading-edges (Ziada and Rockwell 1982; Kaykayoglu and Rockwell 1985); and Karman vortex street of an upstream body interacting with a downstream elliptical-edge (Gursul and Rockwell 1990). Vortex-airfoil interactions were also simulated by oscillating an upstream airfoil, hence generating a vortex which subsequently interacted with the downstream wing (Wilder and Telionis 1998; Peng and Gregory 2015, 2017). There are many experimental studies that produced periodic travelling gusts by oscillating airfoils or cascade of airfoils (Gilman and Bennett 1966; Booth and Yu 1986; Brion et al. 2015; Wei et al. 2019a, 2019b; Wu et al. 2020), and by oscillating flaps (Jones and Moore 1972; Bicknell and Parker 1972).

We note that all the previous experimental studies assume nominally two-dimensional incident vortices, although this

has never been confirmed. This is highly relevant to the present study in which two-dimensional vortices interact with airfoils and wings. Recently, Turhan et al. (2022) investigated the spanwise coherence and correlation length scale of the incident unsteady wakes shed from a periodically plunging upstream airfoil at a Reynolds number based on the chord length of $Re = 20,000$. It was concluded that the Strouhal number is the most important parameter that determines the degree of two-dimensionality of the wake. The Strouhal number based on the peak-to-peak amplitude can be considered as the ratio of the maximum plunge velocity to the freestream velocity, i.e. $V_{pmax}/U_\infty = \pi St_A$. Using the findings of Turhan et al. (2022), it can be assumed that spanwise vortices are quasi-two-dimensional for $V_{pmax}/U_\infty \geq 0.15$ and $x/c \leq 4$ at $Re = 20,000$. Turhan et al. (2022) furthermore discussed the implications for experimental gust generators using oscillating airfoils. In the present experiments, we were able to produce nearly-two-dimensional single vortices.

The vortex-airfoil interactions may be representative of the interactions with high aspect ratio wings, where the tip effects are confined to a small region, and therefore negligible. However, with decreasing aspect ratio of the wing, the three-dimensional effects may become more important. Even if the vortex is nominally two-dimensional, spanwise variations in the gust-wing interaction may lead to different flow physics than the parallel vortex-airfoil interaction. In this paper, we focus on the effect of the wing-tip for a finite wing and oblique gust-wing interactions for a swept wing. Oblique gusts, finite span of the wings and the existence of wing-tip vortices may introduce significant three-dimensional aspects. We investigate these effects by starting with the two-dimensional airfoil case and then examining a finite unswept wing and a finite swept wing.

We expect that the existence of a tip vortex and resulting induced velocity (downwash) will influence the flow separation from the wing leading-edge and the formation of the LEV during the gust encounter. This is based on the observations of plunging wings, which have qualitative similarities with the interaction of vortical gusts. The anchoring of the leading-edge vortex near the wing tip affects the spanwise loading (Son et al. 2022). In addition to the strong three-dimensionality of the LEV, rapid deformation of the incident gust is also possible due to the mutual induction between the LEV and the incident vortex, resulting in the deformation of the incident vortex filament. Complex interactions between the tip vortex and the incident vortex were observed in the numerical simulations for a finite wing with the aspect ratio $AR = 4$ (Barnes and Visbal 2019).

In the case of oblique vortex-wing interactions as sketched for a swept wing in Fig. 1a, the nature of the leading-edge separation, hence the characteristics of the LEV may change. For sufficiently large angles between the vortex and wing, one may expect the formation of an attached

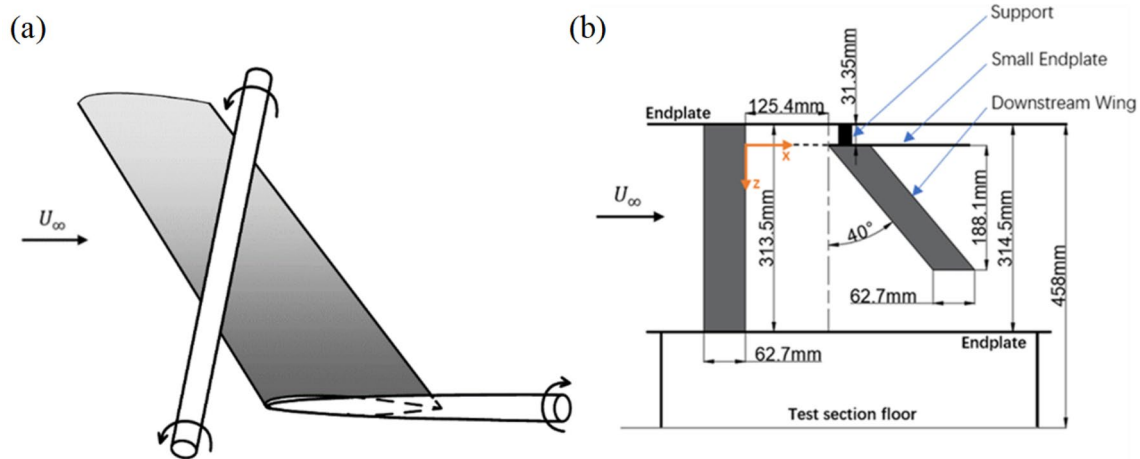


Fig. 1 **a** Schematic of the two-dimensional vortex interacting with a swept wing; **b** experimental setup showing the upstream plunging airfoil and downstream swept wing

LEV, which is very much like a delta wing vortex, rather than a shed and convected vortex. This scenario may occur for the oblique incident gusts in the freestream or for swept wings. The possibility of observing attached LEVs rather than shed LEVs stems from the previous experiments on plunging swept wings (Gursul and Cleaver 2019). This may depend on the sweep angle and the gust amplitude. Barnes and Visbal (2019) numerically simulated a swept wing with the sweep angle $\Lambda = 30^\circ$ and the aspect ratio $AR = 4$. For this small angle of attack ($\alpha = 4^\circ$) and the offset distance of the vortex from the wing, the interaction appeared to spread to the outboard sections of the wing as the vortical gust encountered the wing gradually.

In this paper, we produced a transient nearly-two-dimensional spanwise vortex behind a plunging airfoil and investigated its interaction with an airfoil, an unswept finite wing with $AR = 6$ and a swept wing with $AR = 6$. In water tunnel experiments, unsteady lift force, Particle Image Velocimetry (PIV), and three-component Volumetric Velocimetry measurements were carried out. The offset distance of the initial vortex location and angle of attack of the wing were varied. The scaling of the peak lift coefficients for the airfoil and the two wings were analysed. Flow physics of the interaction, including the vortex stability, turbulent diffusion, and spanwise flow through the cores of the incident vortex and the leading-edge vortex were discussed.

2 Experimental methods

2.1 Experimental setup

The experiments were conducted in a closed-loop water tunnel (Eidetics model 1520) located at the University

of Bath. The test section of the facility is 381 mm wide, 508 mm high, and 1520 mm long, and the freestream velocity can be varied in the range of 0 to 0.5 m/s with a turbulent intensity smaller than 0.5% (Heathcote 2006). The schematic of the stationary wing placed downstream of the plunging airfoil (vortex-generator) is shown in Fig. 1b. Both the upstream plunging airfoil and downstream wing were mounted vertically in the water tunnel. The upstream airfoil was attached to a moving mechanism mounted to a fixed platform and supported by four air bearings and placed at the top of the water tunnel in the test section. With the end-plates at both ends, the airfoil is subjected to a transient plunging motion to generate a single vortex that travels downstream with approximately freestream velocity. The downstream wing has its own smaller end-plate near the root. This end-plate is parallel to and offset from the end-plate of the upstream airfoil. This is done in order to avoid the small region near the end-plate of the airfoil where the vortex is likely to be distorted.

In Fig. 1b, the downstream wing is the swept finite wing with the sweep angle of $\Lambda = 40^\circ$. We also tested an unswept finite wing ($\Lambda = 0^\circ$) as well as an airfoil (in this case a second end-plate was placed at the other end of the wing). Both wings have a semi-aspect ratio of $sAR = 3$ (equivalent to a full aspect ratio of $AR = 6$). The Reynolds number based on the chord length was $Re = 20,000$. Both upstream airfoil and downstream finite wings have a cross-sectional profile of NACA 0012 and the same chord length of $c = 62.7$ mm. The coordinate system is also shown in Fig. 1b. The origin is at the trailing-edge of the airfoil, while $z = 0$ is at the root of the downstream wing.

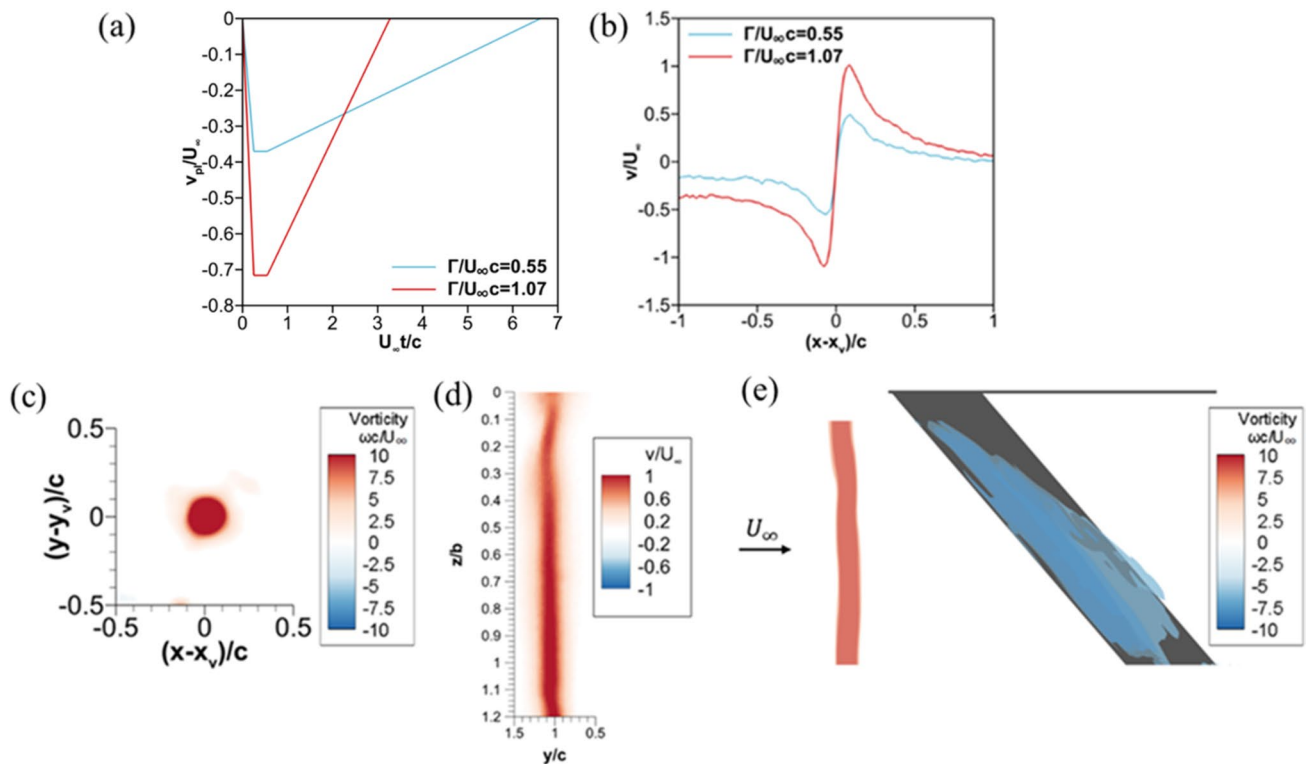


Fig. 2 **a** Time-history of plunging motions; **b** vortex velocity profiles at $U_\infty t/c=2$; **c** spanwise vorticity in midspan plane; **d** cross-stream velocity in crossflow plane; **e** vorticity isosurfaces $\omega c/U_\infty = \pm 6, \pm 9, \pm 12$ for $\Gamma/U_\infty c = 1.07, U_\infty t/c = 2$

2.2 Vortex generation

The upstream airfoil was plunged downwards at the mean angle of attack $\alpha = 0^\circ$ in a transient motion. Figure 2a illustrates the plunge velocity history of the transient plunging motions. The plunging speed of the airfoil is increased fast and then decreased slowly before coming to a complete stop. When the plunge velocity is high a counter-clockwise vortex is generated, whereas there is no roll-up of vorticity shed from the trailing-edge when the plunge velocity is low.

The concept of rapid pitching up of an airfoil to generate leading-edge vortices (Wilder and Telionis 1998; Peng and Gregory 2015, 2017) is not new as discussed in the Introduction. However, separated flow and large wake at the final angle of attack often have large disturbances that ultimately cause three-dimensionality and dissipation of the vortices generated. In contrast, we generate trailing-edge vortices that are more stable and more two-dimensional. In our case, the final geometric angle of attack at the end of the transient motion is zero, ensuring minimum wake disturbances. As the leading-edge is rounded and the trailing-edge is much sharper, we expect that the trailing-edge vortex will be much stronger than the leading-edge vortex (Cleave et al. 2012, 2013). The latter dissipates quickly and cannot be captured downstream

of the trailing-edge. In addition, we made sure that the acceleration part of the plunge motion is sufficiently rapid, which ensures high coherence and two-dimensionality of the vortices (Turhan et al. 2022). The slow deceleration of the airfoil ensures that the opposite sign of vorticity shed does not roll up. The asymmetric profile of the plunge velocity (fast acceleration followed by slow deceleration) effectively generates a single counter-clockwise vortex with minimum wake disturbance.

A counter-clockwise vortical gust is likely to be the worst case as it increases the effective angle of attack as it approaches the wing. The roll-up of the vortex appears to be complete by $U_\infty t/c = 2$. The phase-averaged cross-stream velocity component across the vortex core is shown in Fig. 2b for two different plunging motions shown in Fig. 2a. The strong vortex has the magnitude of the maximum vortex velocity around the freestream velocity. The vortex core radius, which is defined as the location of the maximum tangential velocity, is approximately $0.06c$. Figure 2c shows the spanwise vorticity in the mid-span plane at the instant $U_\infty t/c = 2$ for the strong vortex, which reveals the nearly circular shape of the vortex after the roll-up. The vortex center is approximately at $1.5c$ downstream of the airfoil trailing-edge. The strength (circulation) of the vortex was found by integrating velocity. The

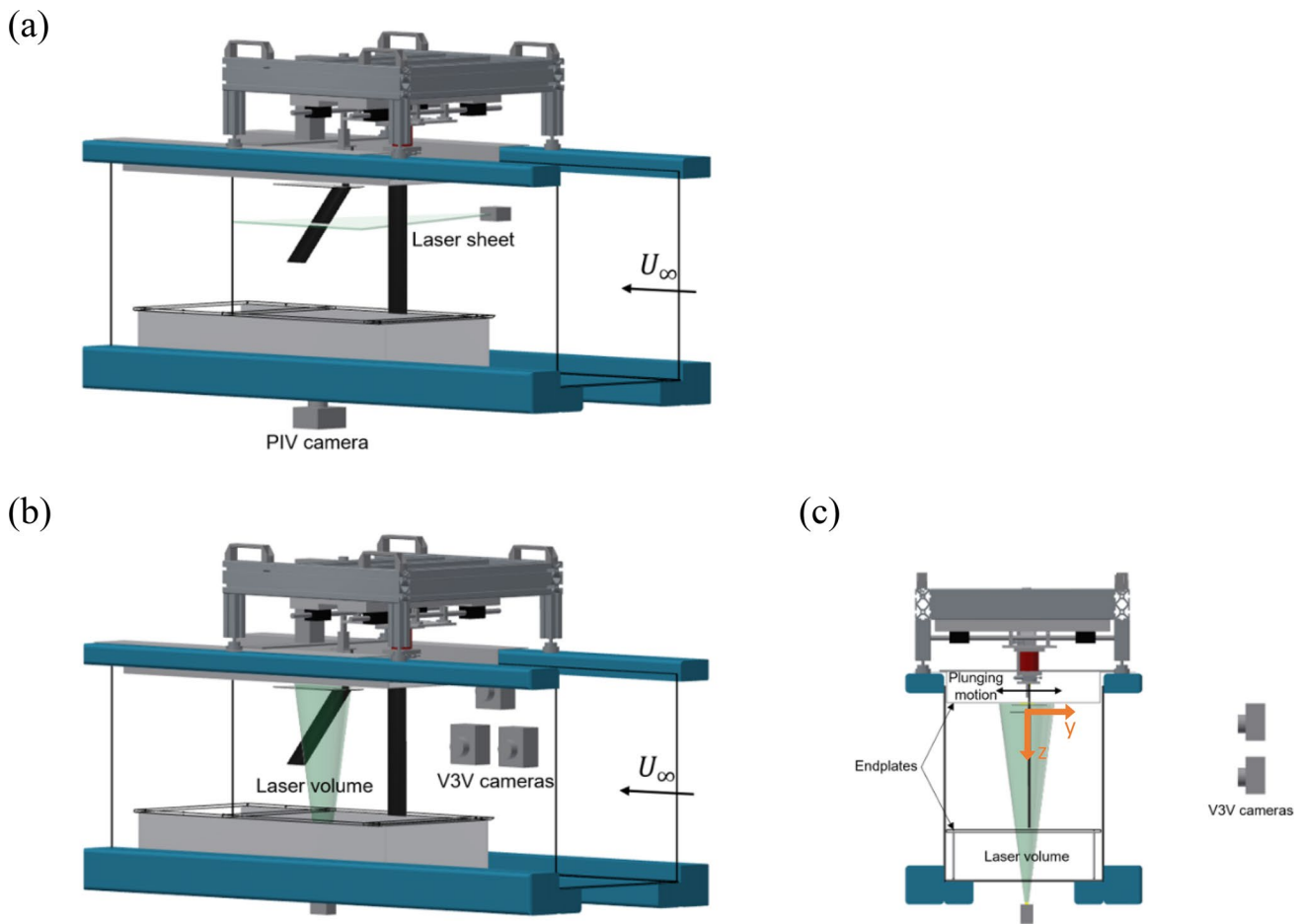


Fig. 3 Setup for **a** PIV (isometric view); **b** Volumetric velocity measurements (isometric view); and **c** upstream view

weak vortex has a circulation of $\Gamma/U_\infty c = 0.55$, while the strong vortex has a circulation of $\Gamma/U_\infty c = 1.07$.

For the strong vortex at $U_\infty t/c = 2$, Fig. 2d shows the phase-averaged cross-stream velocity component in a crossflow plane that is located at one vortex radius from the vortex center. The cross-flow velocity is fairly independent of the spanwise distance, confirming its nearly two-dimensional structure. This is consistent with the findings of Turhan et al. (2022). Their data for the same chord Reynolds number and in the same downstream region suggest that the spanwise vortices are nearly two-dimensional for the normalized maximum plunge velocity $V_{pmax}/U_\infty \geq 0.15$. In the present experiments, we have $V_{pmax}/U_\infty = 0.37$ and 0.72 (see Fig. 2a). There is a slight non-uniformity for small values of the spanwise coordinate. Unfortunately, we could not avoid using this region by increasing the offset distance of the wing root end-plate from the end-plate of the airfoil, which would mean a smaller distance from the wing-tip to the wall of the test section. Figure 2e presents the phase-averaged spanwise vorticity iso-surfaces for the strong vortex at $U_\infty t/c = 2$, when the swept wing is placed

downstream. The isosurfaces in this graph were obtained by interpolation of the spanwise vorticity data measured at ten spanwise planes using the PIV method. The phase-averaged vortex is nearly-two-dimensional upstream of the wing. For the unswept wing and the airfoil experiments, we placed the airfoil or wing at the same streamwise location as the mid-span cross-section of the swept wing in Fig. 2e.

2.3 Particle image velocimetry measurements

Figure 3a shows the arrangement for the two-dimensional particle image velocimetry measurements. The PIV system (TSI) consists of a synchroniser (TSI model 610036), a double-pulsed laser (ND: YAG 50 mJ, repetition rate 3.75 Hz), and an 8MP (3320*2496) Powerview Plus CCD camera with a Nikkor 50 mm f/1.8D lens. The camera has a field of view of 313×235 mm. Hollow glass spheres (8–12 μm) were used as seeding particles in the experiments. Phase-locked PIV measurements were conducted with a total of 60 image pairs taken for each selected phase during the transient motion of the upstream airfoil. The images were processed by the

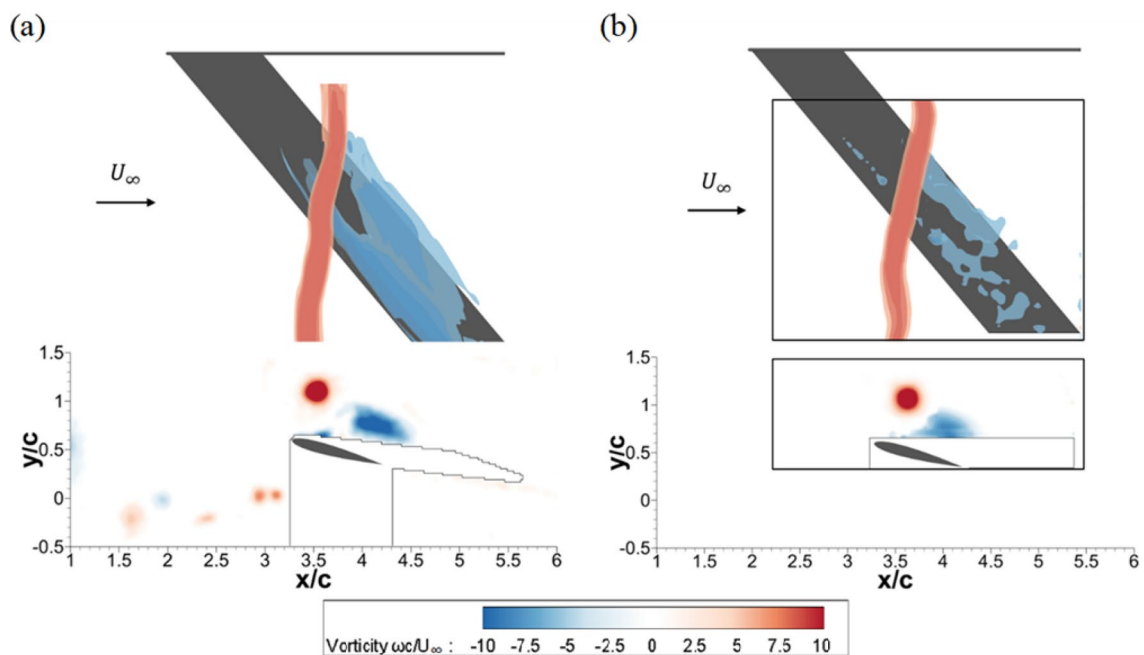


Fig. 4 **a** PIV; **b** Volumetric 3-component velocity measurements: iso-surfaces of spanwise vorticity $\omega c/U_\infty = \pm 6, \pm 9, \pm 12$ (top) and the spanwise vorticity at the mid-span plane, for strong vortex $\Gamma/U_\infty c = 1.07$, $\varepsilon = 0.4$, $\alpha = 15^\circ$

Insight 4G with an interrogation window size of 32 by 32 pixels with 50% overlapping, resulting in a spatial resolution of $2.5\%c$. The estimated uncertainty for velocity measurements was 2% of the freestream velocity U_∞ . The coordinate system is also shown in Fig. 3c. Phase-averaged PIV measurements were conducted in the mid-span plane for the unswept wing and the airfoil, and at ten spanwise planes ($z/b = 0.1, 0.2, \dots, 1.0$) for the swept wing at 8 phases for the transient plunging motion of the upstream airfoil. The phases were selected between $U_\infty t/c = 2$ and 5.5, with an increment of 0.5.

2.4 Volumetric 3-component velocimetry measurements

Figure 3b and c show the arrangement for the three-dimensional volumetric 3-component velocimetry measurements. The V3V system (TSI) includes a double-pulsed laser (ND: YAG 200 mJ, repetition rate 3.75 Hz), and three 4MP (2048*2048) 12 bit CCD cameras with Nikkor 50 mm f/1.8D lenses. The cameras were mounted on a dedicated frame (TSI V3V-9000-CS) and the same synchroniser as in the PIV measurements was used. Each measurement volume has a field of view of $140 \times 140 \times 100$ mm. In the present study, four separate volumes were used for the swept wing cases and two volumes were used for the unswept wing and airfoil cases. The data for multiple volumes were collected separately and then the volumes were merged by using reference points on the wing or airfoil. Seeding was done using

polyamide seeding particles with a size of 50 μm diameter. Images were processed by Insight V3V with an interrogation volume of $8 \times 8 \times 8$ mm with 50% overlapping, resulting in a spatial resolution of 4 mm ($6.4\%c$). The uncertainty for the volumetric measurements is estimated as 3% of U_∞ . Similar volumetric velocity measurements in the same facility were reported by Calderon et al. (2013a, 2013b), who provided the details of the method. In the current setup, the same phases of the measurements were selected as in the PIV measurements. For each phase, 60 phase-locked images were taken, and the phase-averaged velocity fields were calculated.

The spatial resolution of the PIV measurements is 2.5 times better than the resolution of the volumetric measurements. However, the latter method provides spatial picture of the vortical structures, including the spanwise flow within the vortices. The PIV and volumetric measurements obtained at different times are compared in Fig. 4 for the same vortex and geometry. At the top, iso-surfaces of the phase-averaged spanwise vorticity are compared at $U_\infty t/c = 4$. At the bottom, phase-averaged spanwise vorticity is compared in the mid-span plane at the same instant. The masked regions for both methods and the field of view for the volumetric method are shown. The agreement for the counter-clockwise incident vortex is reasonable. However, weaker spanwise vorticity shed from the wing for the volumetric measurements is due to the poorer resolution. In summary, the PIV measurements offer better resolution and a larger field of view, whereas the volumetric

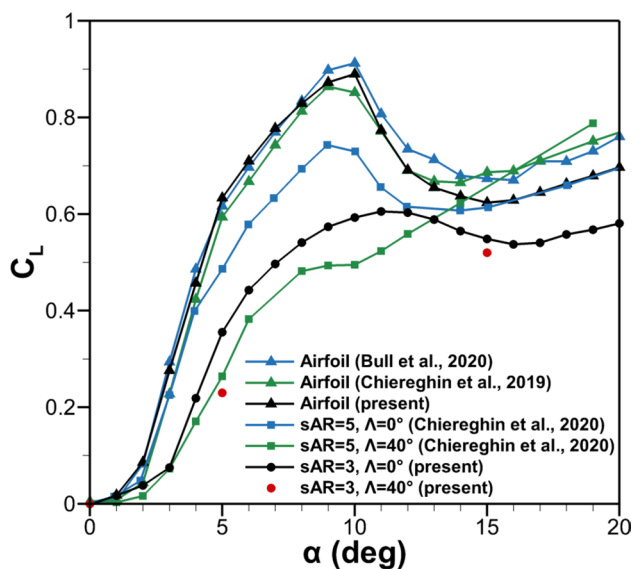


Fig. 5 Lift coefficient as a function of angle of attack in freestream for the airfoil, unswept wing and swept wing, and comparisons with the literature at $Re = 20,000$

measurements offer insight to the spanwise flow in the vortices. We used both methods in a complementary way for the finite wings.

2.5 Force measurements

A single component binocular type load cell was utilized to measure the lift force on the downstream wing. The load cell was connected to the downstream wing support shown in Fig. 1b. The force data were filtered with a 20 Hz Butterworth low-pass filter to reduce the noise. For each experiment, force data were acquired at a sampling frequency of 2000 Hz for the same total duration in each test and then averaged from 20 cycles. For the lift force in freestream as shown in Fig. 5, the force data were sampled at 1000 Hz for 60 s. Figure 5 shows the lift coefficient as a function of angle of attack for the airfoil, unswept wing, and swept wing at $Re = 20,000$, and compares it with the other data for airfoils and wings at the same Reynolds number (Bull et al. 2020; Chiereghin et al. 2019, 2020). For the force measurements, the errors in calculating the lift coefficient C_L are attributed to the uncertainty of the lift force L , the freestream velocity U_∞ , the water density ρ , and the wing planform area S . Using the standard error propagation procedures described by Moffat (1988), the experimental uncertainty of C_L was estimated to be less than 5%. At this Reynolds number, for all airfoils and wings, the low-Reynolds number effects and nonlinear lift slope at small incidences are evident.

3 Results and discussion

3.1 Unloaded airfoils and wings ($\alpha = 0^\circ$)

3.1.1 Airfoil and finite unswept wing

Initial PIV measurements in the mid-span plane of the unswept wing and the airfoil showed that the unsteady flows, including vortex trajectories, are qualitatively similar (Qian 2022). Subsequent measurements of the lift force confirmed that a simple correction for the downwash of the finite wing is sufficient. Consequently, we carried out most of the detailed PIV measurements in the mid-span plane of the unswept wing. The normalized offset distance, defined as $\varepsilon = (y_{VI} - y_{LE})/c$, was varied. Here, y_{VI} is the initial cross-stream location of the vortex (the initial time is taken as $U_\infty t/c = 2$ when the first measurements of the traveling vortex is taken) and y_{LE} is the cross-stream coordinate of the leading-edge of the wing (see the inset in Fig. 6). This figure presents the vortex trajectory by superimposing the vorticity fields at eight phases between $U_\infty t/c = 2$ and 5.5 for the unswept wing. The left column shows example cases for the weak vortex and the right column presents the cases for the strong vortex. In all cases, including the case of the head-on collision, there is a mild separation from the wing for the unloaded wing. For the negative offset distance, as well as for the zero offset, the trajectory of the counter-clockwise incident vortex is deflected downwards, rather than remaining nearly parallel to the freestream as for the positive offset cases. This is due to the larger separation region that develops over the lower surface of the wing as will be discussed later.

The most important observation is that the phase-averaged vortices become more diffused as they interact with the wing, especially for strong interactions. This occurs for larger circulation or smaller offset ε . The variation of the circulation of the incident vortex at different times is shown in Fig. 7. The circulation is calculated based on the method described by Cleaver et al. (2011). A square path line around the incident vortex is defined in the flow field obtained by PIV measurements. The center of the square coincides with the vortex center which is defined as the location of the maximum vorticity. The square is then expanded by one spatial unit at a time and the circulation is calculated by performing line-integration until the increase of the magnitude of circulation is small (less than 1%).

For both vortices, the circulation remains roughly the same or decays very slowly if the vortex travels at a distance from the wing, indicating weak interaction. In contrast, if the vortex becomes closer to the wing, much more rapid decay of the circulation is evident, which starts

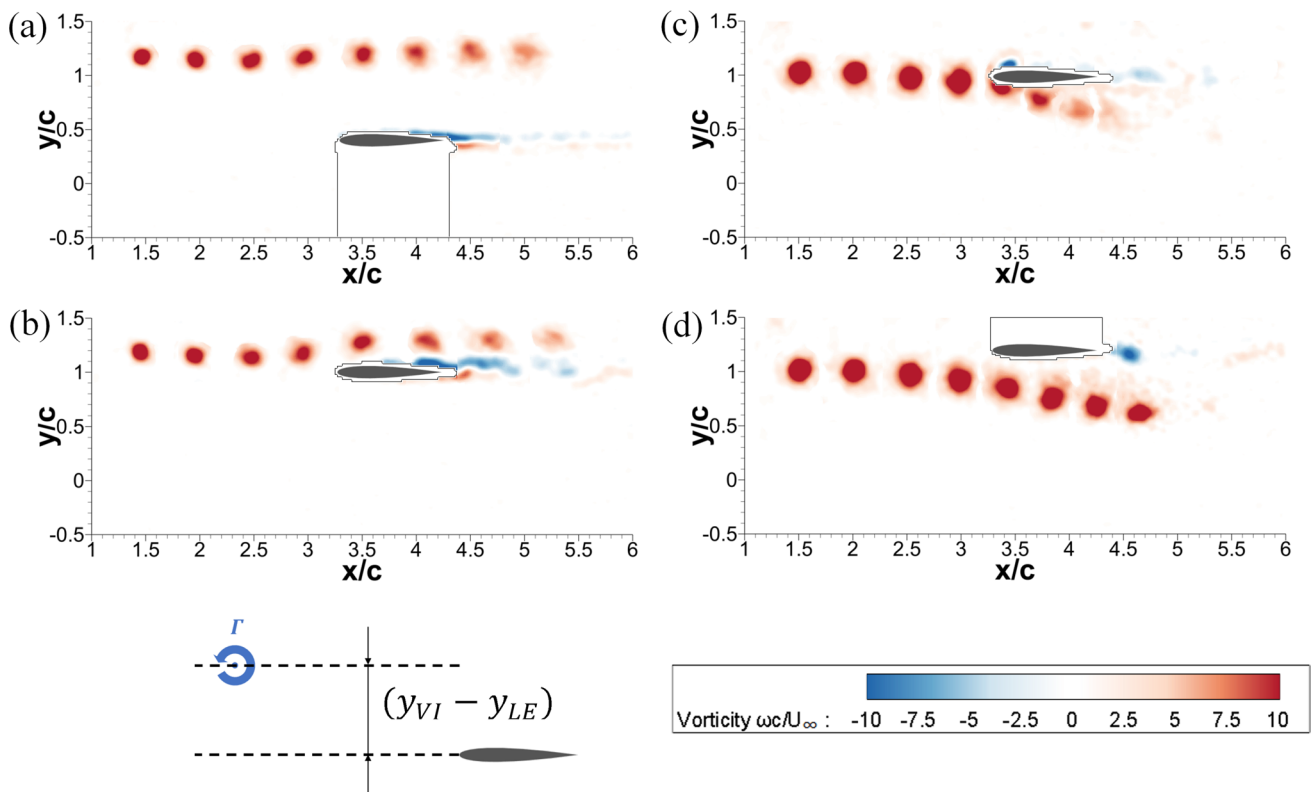


Fig. 6 Vortex trajectories for weak vortex $\Gamma/U_\infty c = 0.55$ (left column) for **a** $\varepsilon = 0.8$, **b** $\varepsilon = 0.2$; strong vortex $\Gamma/U_\infty c = 1.07$ (right column) for **c** $\varepsilon = 0$, **d** $\varepsilon = -0.2$

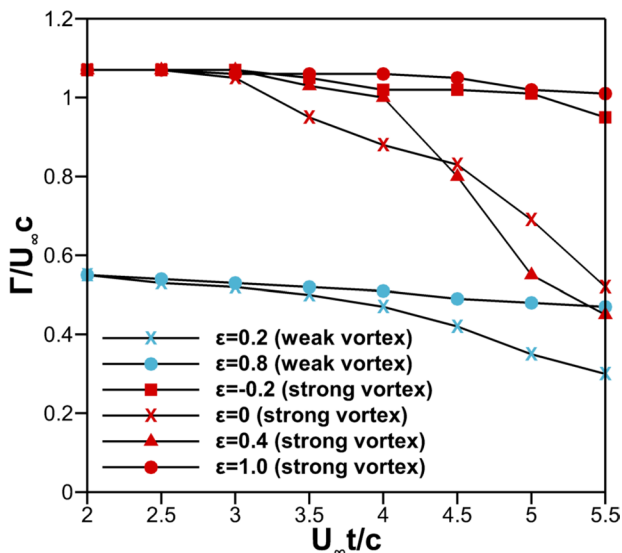


Fig. 7 Circulation of incident vortex during interaction with unswept wing, $\alpha = 0^\circ$

around $U_\infty t/c = 3.5$. (The only exception to this trend is the case of $\varepsilon = -0.2$ (shown in Fig. 6d) for which the decay of the circulation appears to be delayed and the reason remains unclear). At $U_\infty t/c = 3.5$, the vortex is just

upstream of the leading-edge. As the calculation of the circulation is extended until it changes less than 1% over a large area, the general decline in the circulation as time advances could not be attributed to the vorticity diffusing outside of the area within which the circulation is being computed. We note that, for the close interactions with the wing, cross-cancellation of the vorticity might contribute to the rapid decay of the circulation.

Similar decay of the circulation of the incident vortex during close interactions with the wing at much higher Reynolds numbers were observed by Peng and Gregory (2015 and 2017). The results in Figs. 6 and 7 suggest that, even for those interactions that are not close such as in Fig. 6a, the incident vortex may be diffused (while the circulation remains less affected) when it starts interacting with the wake of the wing. We note that these observations are valid for the phase-averaged vortex. The diffused nature of the phase-averaged vortices is likely to be due to the increasing three-dimensionality of the instantaneous vortices. It is well known that isolated two-dimensional vortices, when subjected to strain, may be unstable to the three-dimensional instabilities (Tsai and Widnall 1976; Waleffe 1990). Theoretical predictions of the wavelength of the three-dimensional instabilities of the isolated vortices were made in several investigations (Eloy and Le Dizès

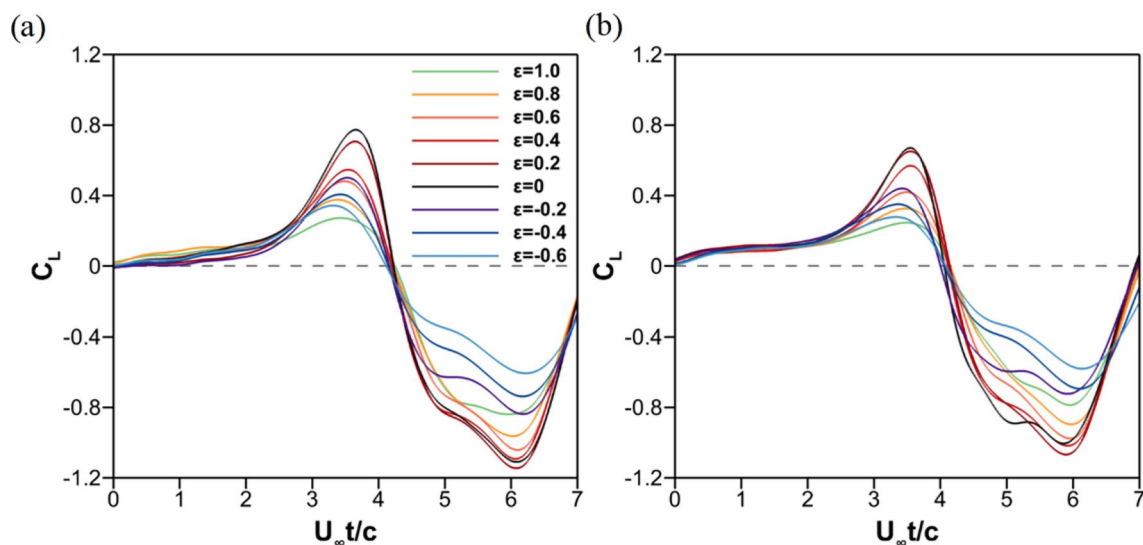


Fig. 8 Time history of the lift coefficient as a function of dimensionless time for **a** airfoil, **b** finite unswept wing; strong vortex $\Gamma/U_\infty c = 1.07$, $\alpha = 0^\circ$

1999; Antkowiak and Brancher 2004; Pradeep and Hussain 2006). A mechanism by which freestream disturbances are transformed into vortex core and excite the vortices has been recently proposed (Bölle et al. 2021). There is also evidence that secondary vortices and trailing-edge vortices cause disturbances for the leading-edge vortices, which are mostly spanwise vortices (Son et al. 2022). In our case, the incident vortices are subject to disturbances due to other vortices or vorticity sheets, separation from the leading-edge, and the wing wake. The existence of the wing and its wake clearly affect the incident vortices.

In Fig. 8, the time history of the lift coefficient for the airfoil and the wing is compared for the normalized offset distances between $\epsilon = -0.6$ and $\epsilon = 1.0$, with an increment of 0.2. Overall, the lift history looks similar for the airfoil and the wing. The lift coefficient is smaller for the wing due to the finite aspect ratio and the induced downwash of the tip vortices, which will be discussed further later. The positive peak lift occurs around $U_\infty t/c \approx 3.5$ for all cases for the airfoil and for the wing, which is due to the same arrival time of the vortex just upstream of the airfoil/wake. This is shown in Fig. 9a with the phase-averaged vorticity and velocity magnitude at the $U_\infty t/c = 3.5$ for the strong vortex $\Gamma/U_\infty c = 1.07$ and $\epsilon = 0$. The incident vortex is just upstream of the wing at this instant (this can be confirmed for other offset distances in Fig. 6 for both vortices). There is no noticeable evidence of flow separation from the leading-edge, while the streamlines around the wing are nearly parallel to the surface. Therefore, the positive peak is likely to be due to the potential flow mechanism. The peak lift coefficients appear to increase with decreasing offset distance. This is also consistent with the assumption of the potential

flow: the induced velocity by the incident vortex on the wing becomes maximum for the head-on collision ($\epsilon = 0$) at this instant and produces maximum effective angle of attack for the wing.

The magnitude of the negative lift peak is larger than the positive peak for the unloaded airfoil and wing. The negative peak is broader and spans longer than one convective time scale. In Fig. 9b, we show the velocity and streamlines at $U_\infty t/c = 5$. The incident vortex is about to reach the trailing-edge of the wing. It is more diffused, but still able to produce a downwash on the wing and also to cause flow separation on the lower surface of the wing. The flow separation suggests that viscous effects are important for the negative lift peak. The viscous effects and the magnitude of the negative peak lift are expected to decrease with increasing angle of attack (loaded wings).

Here, we develop a simple reduced order model to predict the positive peak lift and how it scales with the offset distance and the circulation of the incident vortex. It is based on the lumped vortex model (LVM) which was used to model the Wagner problem (Katz and Plotkin 2001). In the model, the incident vortex is released at the most upstream location for which we have the PIV data for and the cross-stream location y_{V1} . We use the vortex location and circulation from the PIV measurement at each instant. In the lumped vortex model, it is assumed that there is no flow separation and vortex shedding from the leading-edge. The Kutta condition at the trailing-edge is assumed to be satisfied by placing the bound vortex (with circulation Γ_b) at the quarter chord. The collocation point is at $0.75c$ (see the inset in Fig. 10). At each time step, a wake vortex with circulation Γ_w is released to satisfy the Kelvin's theorem. The wake vortices are convected with the freestream

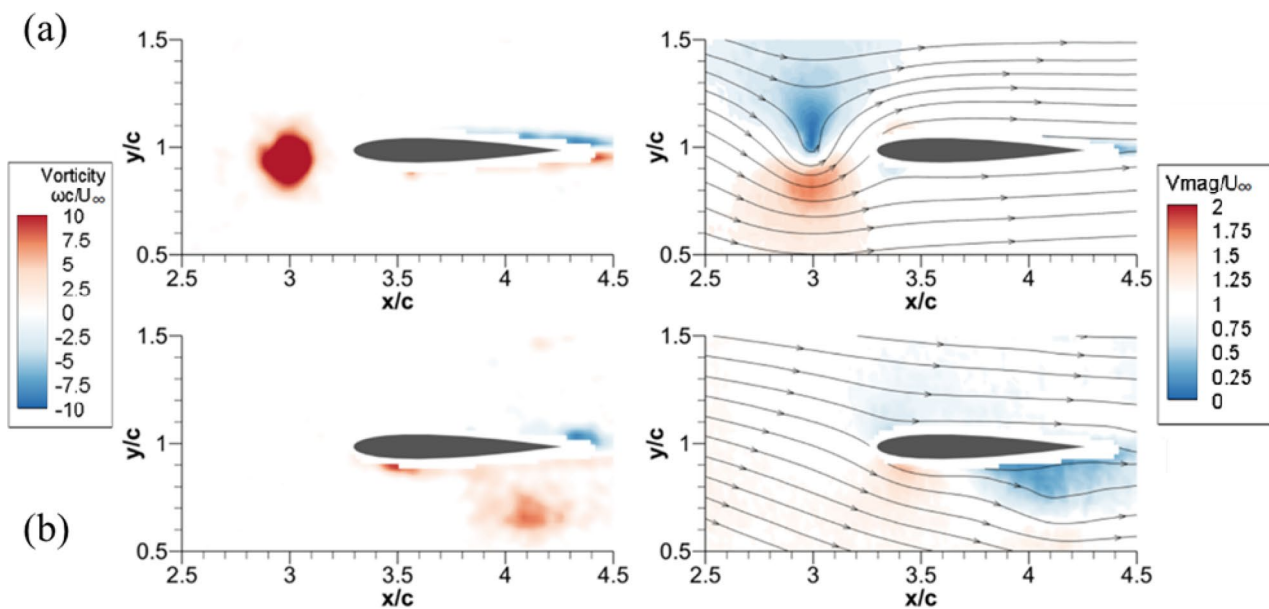


Fig. 9 Vorticity (left) and velocity magnitude with streamlines (right) at **a** $U_\infty t/c = 3.5$, **b** $U_\infty t/c = 5$; strong vortex $\Gamma/U_\infty c = 1.07$, $\epsilon = 0$, $\alpha = 0^\circ$

velocity. In addition, the zero normal flow boundary condition is satisfied at the collocation point at the plate’s three-quarter chord point, considering the bound vortex, induced velocity of the incident vortex, and the wake vortices. The Kelvin’s theorem together with the zero normal flow condition are used to calculate the strength of the newly released wake vortex and the instantaneous value of the bound vortex.

The lift per unit span (Katz and Plotkin 2001, page 384) is then calculated from

$$L' = \rho \left[U_\infty \Gamma_b + \frac{\partial}{\partial t} \Gamma_b c \right]$$

which includes two terms: $\rho U_\infty \Gamma_b$ (quasi-steady lift) and $\rho \frac{\partial}{\partial t} (\Gamma_b c)$ (unsteady contribution). In calculating the total lift force, we made an aspect-ratio correction, using the Prandtl’s lifting line theory and assuming an elliptical circulation variation, as the PIV data for the finite wing was used as input. Given the assumptions, the LVM predicts the lift time history qualitatively for two different cases in Fig. 10a. The positive peaks are overpredicted, whereas the negative peaks are underpredicted, perhaps due to the inability of capturing the viscous effects for the negative lift. The qualitative variation of the lift, the timings of the positive peaks, and the timing of the zero-lift are in reasonable agreement. The model captures the essential features and supports the assumption of the potential flow for the positive peak. (As noted earlier, the negative peaks, which are viscous-dominated, become less important with increasing angle of attack).

We made further assumptions in the lumped vortex model to predict the positive peak. The vortex trajectory remains

parallel to the freestream at the initial release location y_{vI} (this assumption is close to the experimental observations). The effect of the wake vortices is numerically small as they convect downstream with freestream, and therefore neglected. Hence, the zero-normal-velocity condition at the collocation point dictates that the bound vortex circulation is proportional to the incident vortex circulation, and also depends on its instantaneous location (x_V, y_{vI}) . It can be calculated as:

$$\Gamma_b = \frac{\Gamma}{2} \frac{(x_V - x_{LE})/c + 0.75}{[(x_V - x_{LE})/c + 0.75]^2 + \epsilon^2}$$

Furthermore, we note that the total lift increases slowly in time as the vortex approaches the wing, at least until the lift becomes maximum. As the predicted quasi-steady lift appeared to be dominant (not shown here) compared to the unsteady effects, we assume that the lift is dominated by the quasi-steady lift:

$$L' = \rho U_\infty \Gamma_b$$

When the lift becomes maximum at $U_\infty t/c = 3.5$, the PIV data suggest that the incident vortex is located just upstream of the wing at a distance as $(x_V - x_{LE})/c = 0.3$. To calculate the total lift, we used the span of the wing b and the correction for the aspect ratio (using the Prandtl’s lifting line theory and assuming an elliptical circulation variation) to arrive at:

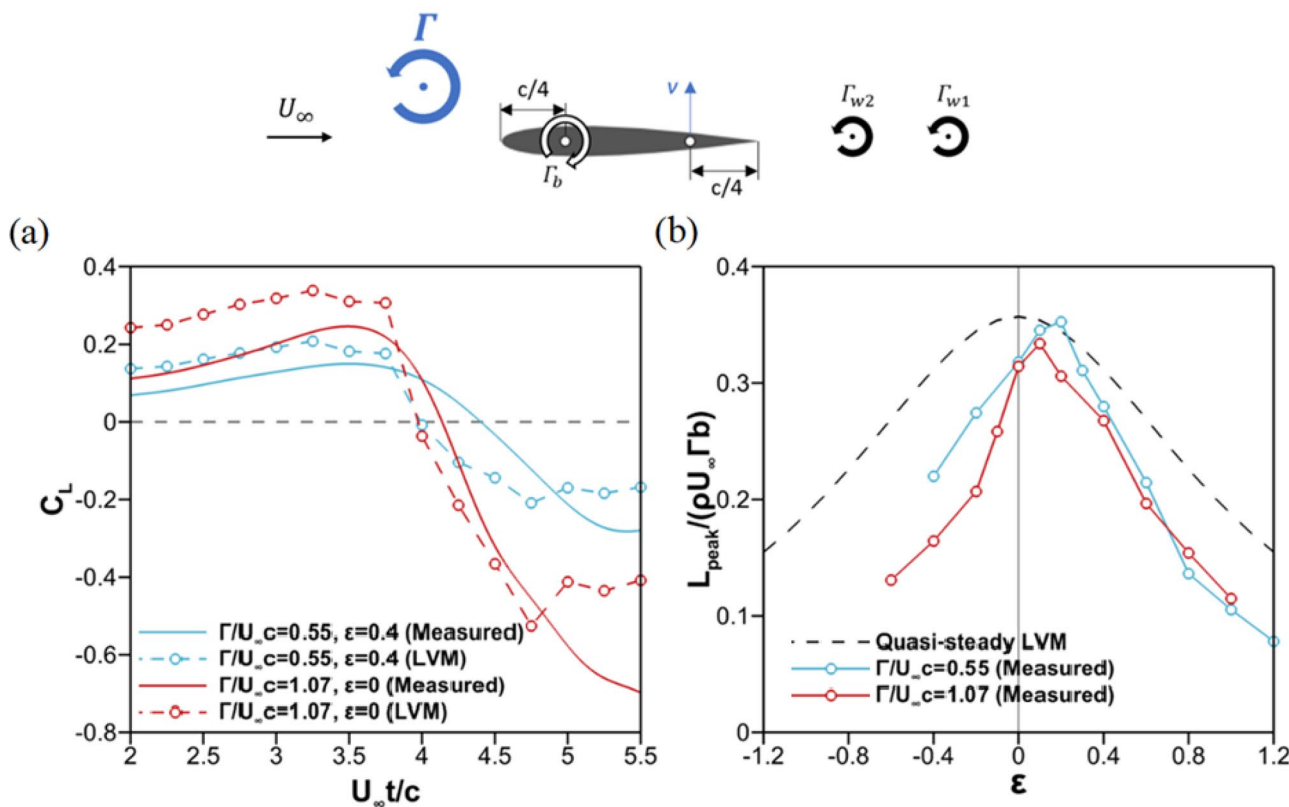


Fig. 10 **a** Comparison of the lumped vortex model (LVM) and measurements for the time history of the lift coefficient for two cases; **b** normalized peak lift force as a function of the normalized offset distance

$$\frac{L_{\text{peak}}}{\rho U_\infty \Gamma b} = \frac{0.39}{1.05^2 + \varepsilon^2}$$

This equation predicts that the maximum lift force is proportional to the circulation of the incident vortex. We note that the circulation is assumed to be constant in the model as there is negligible change in the circulation until the instant of the positive lift peak in the experiments (see Fig. 7). In contrast, the same cannot be said for the negative lift peak during which the circulation may decrease for close interactions. Interestingly, the viscous simulations of Martínez-Muriel and Flores (2020) at a low Reynolds number of $Re = 1000$ also predicts that the maximum lift change due to the interaction is roughly proportional to the incident vortex circulation. Our prediction is plotted with dashed lines in Fig. 10 and compared with the measurements. For the two incident vortices we tested, the experimental data appear to collapse well. The agreement with the low order model is fair for small offset distances, but becomes poor with increasing offset distances, particularly at the negative offset distances (vortex travelling over the lower surface of the wing) due to the stronger viscous effects.

Although the prediction of the low order model is symmetric in Fig. 10b, the measurements show that there is slight asymmetry. The largest positive lift occurs at $\varepsilon = 0.1$ for the strong vortex and at $\varepsilon = 0.2$ for the weak vortex. Similar asymmetries for a symmetric airfoil at higher Reynolds numbers were reported, with maximum pressure fluctuations occurring at small offset distances (Peng and Gregory 2017). This asymmetric effect can be explained by the different viscous response of the boundary layers on the upper and lower surfaces when the vortex passes over. When the counter-clockwise vortex passes over the upper surface, the boundary layer flow is accelerated due to the induced velocity of the incident vortex. In contrast, when the incident vortex passes over the lower surface of the wing, its induced vortex decelerates the boundary layer and causes flow separation as shown in Fig. 9b.

Figure 11a, b show the variation of the maximum lift coefficients for the airfoil and the finite wing as a function of the normalized offset distance. For both vortices, the variations for the airfoil and the wing, including the local maximums at small nonzero offset distances, are similar. The maximum lift for the wing is smaller due to the downwash of the wing-tip vortex that develops during the interaction over the wing at $\alpha = 0^\circ$.

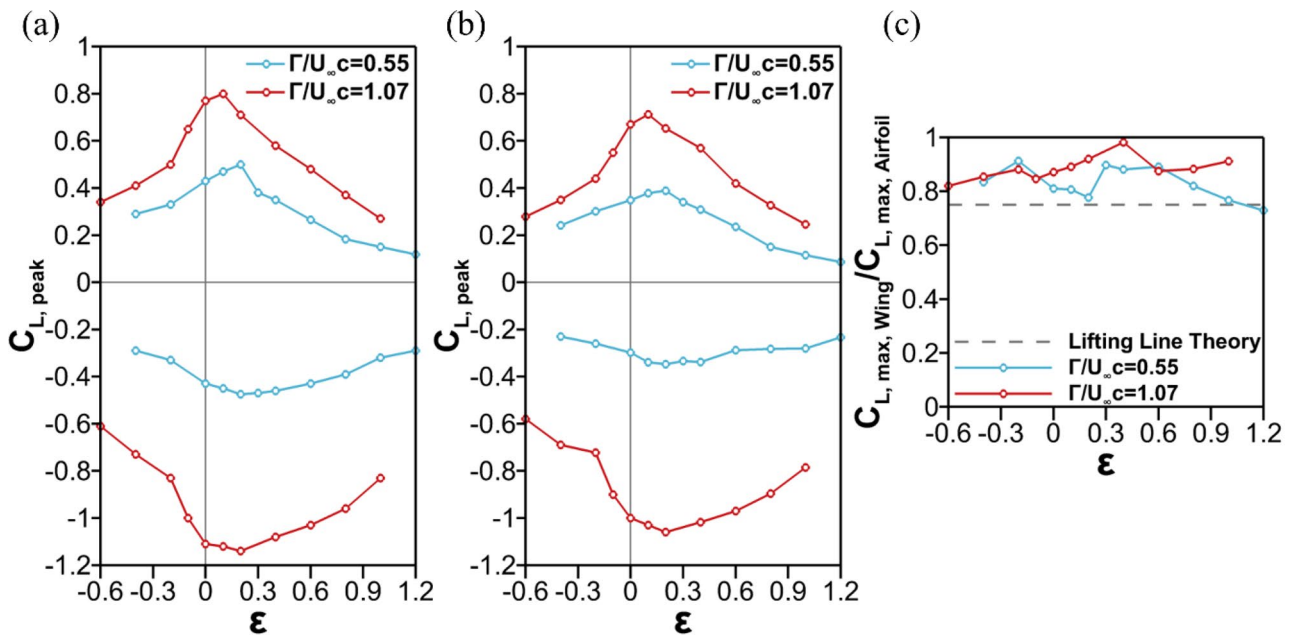


Fig. 11 Peak lift coefficients for **a** airfoil, **b** finite unswept wing, and **c** the ratio of the peak lift of the wing and the airfoil, $\alpha = 0^\circ$

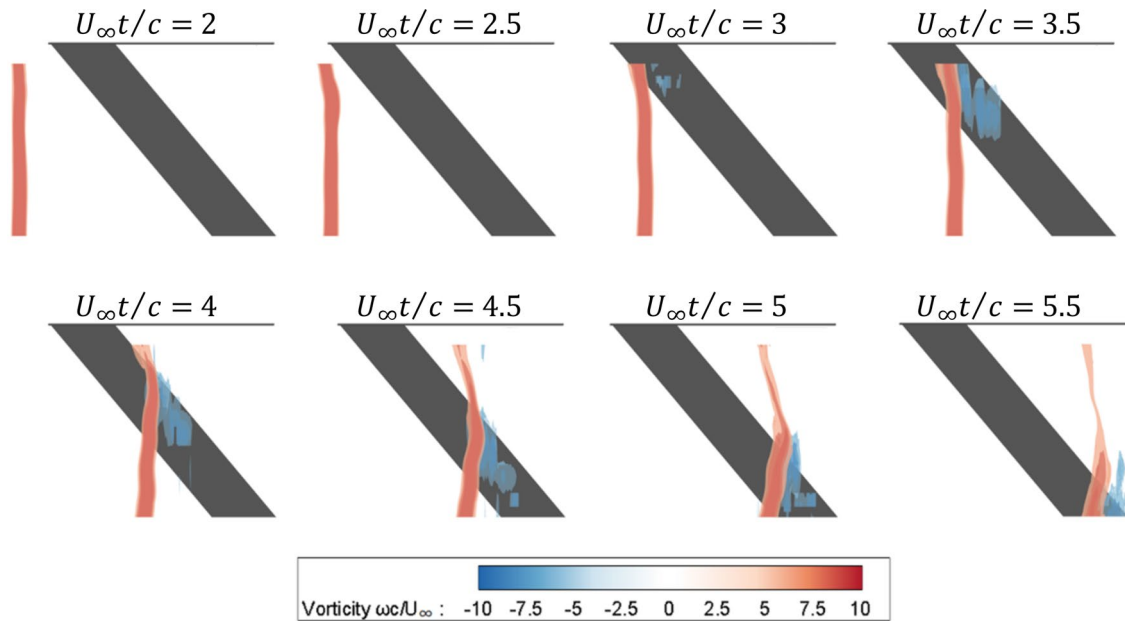


Fig. 12 Iso-surfaces of spanwise vorticity $\omega c/U_\infty = \pm 6, \pm 9, \pm 12$ from the PIV data; strong vortex $\Gamma/U_\infty c = 1.07, \epsilon = 0.4, \alpha = 0^\circ$

The ratio of the positive lift peaks for the wing/airfoil for which we presented a low order model earlier is shown in Fig. 11c. As expected, the ratio is almost always less than unity. For our low order model, the ratio of the maximum lifts is shown with the horizontal dashed line in this figure and corresponds to the aspect ratio correction. This correction is derived from the lifting line theory, which is

developed for steady aerodynamics. It is interesting that the measured lift ratios are not too far away from the quasi-steady prediction. This is consistent with our assumption of quasi-steady flow for the positive peaks.

3.1.2 Swept wing

Iso-surfaces of spanwise vorticity obtained from the PIV measurements and interpolated are shown in Fig. 12 at different times $U_\infty t/c$ for the strong vortex $\Gamma/U_\infty c = 1.07$, $\varepsilon = 0.4$, $\alpha = 0^\circ$ and the swept wing ($\Lambda = 40^\circ$). The incident vortex interacts with the wing near the root first and then gradually at outboard wing sections later. One can see the opposite sign of vorticity (in blue) downstream of the incident vortex, which suggests weak separation on the wing as the angle of attack is zero. As the vortex filament interacts with the wing, the part above the wing induces local flow separation while multiple vortices (in blue) shed from the wing that are parallel to the incident vortex (this is most visible at $U_\infty t/c = 3.5$). Meanwhile, the inboard part of the incident vortex filament diffuses rapidly as soon as it is above the wing wake. This produces a partially diffused vortex inboard and still coherent vortex outboard. We do not have measurements of the flow in the spanwise direction from 2D-PIV measurements at multiple spanwise planes. However, there is no evidence of significant spanwise flow in the incident vortex in the volumetric measurements that will be presented for the loaded wings later. In summary, the interaction presented in Fig. 12 can be described as a local interaction of the vortex filament with the parts of the wing. This suggests that a strip theory approach in which for each local section there is a two-dimensional interaction may be appropriate.

Figure 13 shows the iso-surfaces of spanwise vorticity superimposed at all measurement times $U_\infty t/c$ for the weak (left column) and strong vortex (right column) and various offset distances. In Fig. 13, for the purpose of clarity, the opposite sign of vorticity due to the weak separation has been excluded. Pseudo-trajectories for all cases exhibit strong three-dimensionality and rapid diffusion of the inboard part of the vortex filaments (and this becomes significant in the near-wake), whereas the outer part remains intact before the interaction with the wing. The approaching incident vortex remains nearly-two-dimensional and shows little diffusion before the interaction, even for the head-on collision case shown in part (d). Overall, Fig. 13 confirms that the interaction appears to be quasi-two-dimensional in the sense that at each spanwise plane the interaction remains unaffected by the other spanwise planes.

We compare the time history of the lift coefficient for various offset distances for the unswept wing and swept wing in Fig. 14a, b, respectively. The most important observations are the decrease of the peak lift, broadening of the positive peak, and the decreasing temporal gradients for the swept wing during the interaction. For the same offset distance, swept wing cases have smaller peaks and a more gradual variation in lift time history. This can be explained by the fact that each spanwise section of the wing experiences the

interaction with the vortex at different times. This results in not only a decrease in the peak lift force, but also a gradual build-up of the lift force until the peak is reached followed by a slower decrease of the lift. We applied the strip theory to the lift data of the unswept wing for each cross-section, while taking into account the different arrival times of the vortex to different locations of the leading-edge in each cross-section, and thus introducing a time delay. This time delay was calculated using the measured convection speed (around $0.99U_\infty$) from the trajectory of the vortex. The total lift was calculated by integrating the local lift at each cross-section. The results of the strip theory shown in Fig. 14c, d capture the essential trends of the swept wing.

The peak lift coefficients for the unswept and swept wings are shown in Fig. 15a, b. The positive peaks are higher for the unswept wing as expected, since the vortex is almost parallel to the leading-edge. In contrast, there is little effect of the wing sweep on the negative lift peaks. Similar magnitudes for both wings are likely to be due to the dominance of the viscous mechanism and flow separation on the lower surface which is caused by the downwash of the incident vortex when it is downstream of the wake. In Fig. 15c, the ratio of the positive peaks is compared for the wings. Here the dashed line corresponds to the ‘‘independence principle’’. This principle relies on the assumption that flow normal to the leading-edge determines the lift (see for example, Kueth and Chow 1998), which implies:

$$\frac{C_{L,\Lambda=40^\circ}}{C_{L,\Lambda=0^\circ}} = \cos^2 \Lambda = \cos^2 40^\circ = 0.59$$

It is interesting that, although the independence principle was developed for steady aerodynamics, the peak lift ratio in our experiments for an unsteady flow is not far away from the prediction of this principle.

3.2 Loaded wings ($\alpha \neq 0^\circ$)

3.2.1 Effect of aspect ratio

For the unloaded wings ($\alpha = 0^\circ$), the main feature was that the flow separation from the wing was negligible during the vortex interaction. We may expect that flow separation from the leading-edge and formation of leading-edge vortices will occur with increasing angle of attack. In Fig. 16 (left column), the vorticity fields at $U_\infty t/c = 5$, when the vortex just passed the airfoil are shown for (a) $\alpha = 0^\circ$, (b) $\alpha = 5^\circ$ (pre-stall), (c) $\alpha = 10^\circ$ (near stall), (d) $\alpha = 15^\circ$ (post-stall), for the weak vortex $\Gamma/U_\infty c = 0.55$ and $\varepsilon = 0.6$. At this instant, the incident vortex is diffused as it is already in the near-wake. For this particular offset distance and the vortex, flow separation and vortex formation are already identifiable at

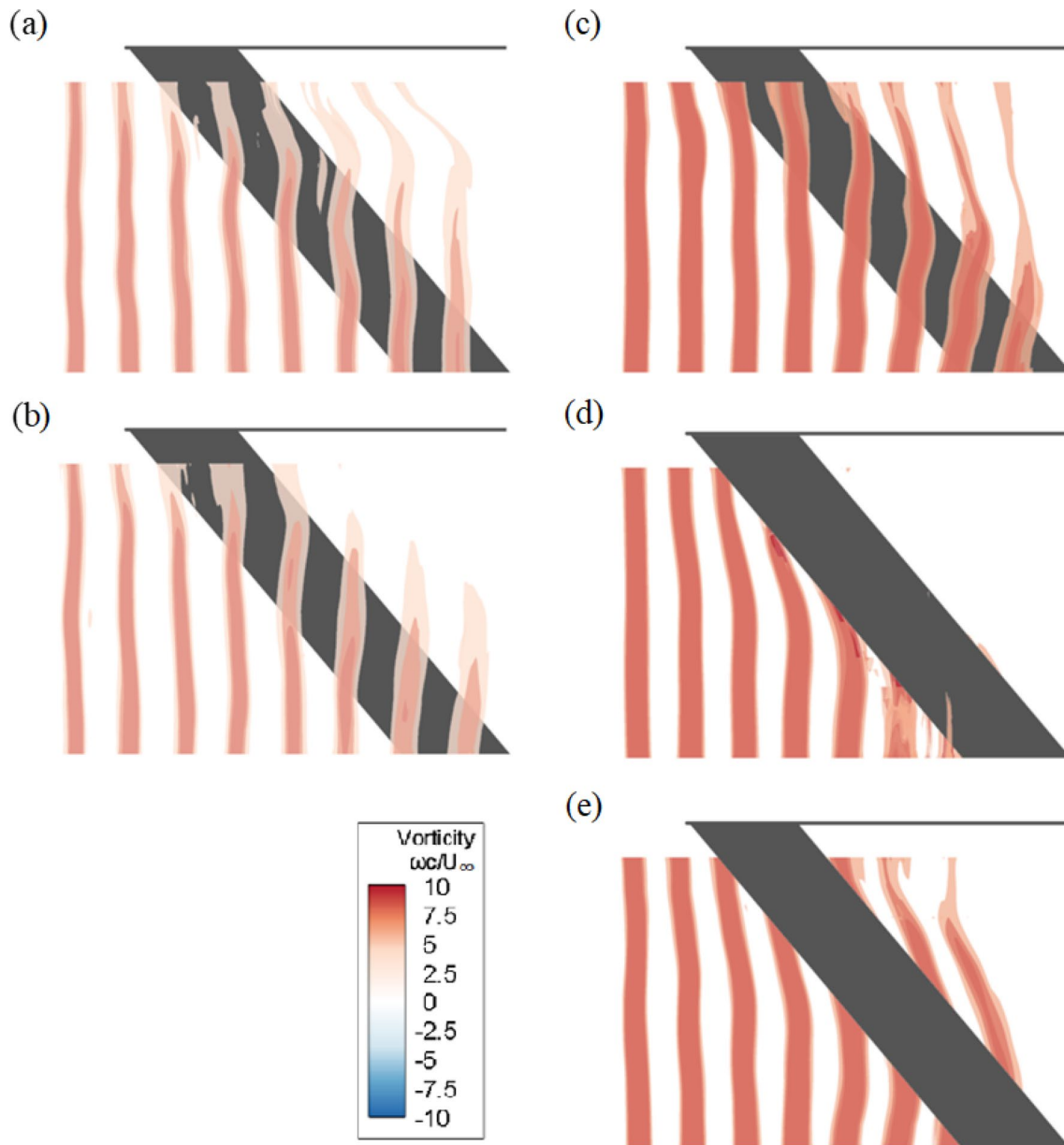


Fig. 13 Iso-surfaces of spanwise vorticity superimposed at all phases for weak vortex $\Gamma/U_\infty c = 0.55$, **a** $\varepsilon = 0.8$ **b** $\varepsilon = 0.2$ (vorticity levels $\omega c/U_\infty = 4, 8, 12$); and for strong vortex $\Gamma/U_\infty c = 1.07$, **c** $\varepsilon = 0.4$, **d** $\varepsilon = 0$, **e** $\varepsilon = -0.2$ (vorticity levels $\omega c/U_\infty = 6, 9, 12$); $\alpha = 0^\circ$; data obtained with the PIV method

$\alpha = 10^\circ$ near the stall angle. With increasing angle of attack, the incident vortex appears to have travelled slightly further downstream. This is likely to be due to the increasing strength of the clockwise bound vortex with increasing angle of attack. At the post-stall angle of attack of $\alpha = 15^\circ$, Fig. 16 reveals clear formation of the leading-edge vortices. In this case, the first LEV forms a vortex couple with the incident vortex and sheds while a second LEV develops. On the right column of Fig. 16, we superimpose the vorticity fields at different times and form trajectories for corresponding angles of attack. In all cases, the diffusion of the incident vortex as

it has passed the airfoil is apparent. Only for the post-stall angle of attack, there is some deviation from being nearly parallel to the freestream and a slight upward deflection of the trajectory due to the separated region on the airfoil.

The volumetric velocity measurements were compared in Fig. 17 for the airfoil and the wing cases at $\alpha = 10^\circ$ and for the same conditions as above (weak vortex $\Gamma/U_\infty c = 0.55$, $\varepsilon = 0.6$). The iso-surfaces of $Q^* = Qc^2/U_\infty^2 = 5, 35, 50, 70$, coloured by spanwise vorticity, is shown at (a) $U_\infty t/c = 3.5$, (b) $U_\infty t/c = 4$, and (c) $U_\infty t/c = 4.5$, for the airfoil (left) and the wing (right). The incident vortex is nearly

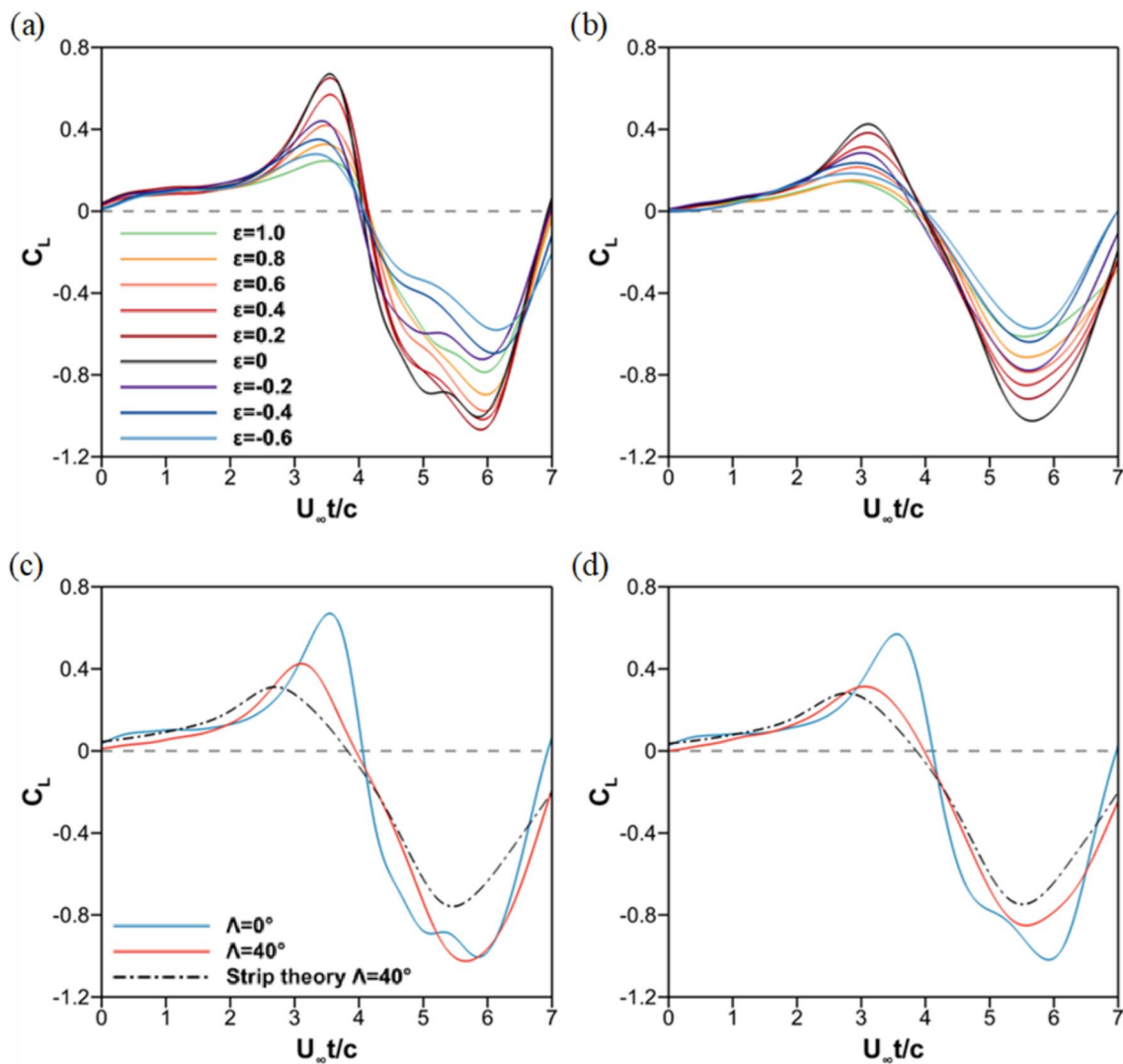


Fig. 14 Lift coefficient time history for **a** unswept wing, **b** swept wing; comparison of the measured lift time history and the strip theory for **c** $\varepsilon = 0$, **d** $\varepsilon = 0.4$. For strong vortex $\Gamma/U_\infty c = 1.07$; and $\alpha = 0^\circ$

two-dimensional throughout the interaction as it approaches and reaches near the trailing-edge for both the airfoil and the wing. The effect of the wing-tip vortex on the incident vortex is not noticeable near the wing-tip. However, the effect of the wing-tip is visible in the development of the leading-edge vortex shedding from the wing. This is best seen underneath the incident vortex in part (b) at $U_\infty t/c = 4$. The LEV is anchored at the wing-tip while the inner part remains parallel to the leading-edge. The shape of the leading-edge vortex filament is very similar to those found for a plunging wing in transient or periodic motion at high reduced frequencies (Son et al. 2022).

Figure 17 also suggests that, at each instant, the incident vortex is slightly slower for the wing (as it is slightly more upstream) than for the airfoil. This is likely to be due to the smaller strength of the bound vortex for the wing. Because

of the finite aspect ratio and the downwash of the tip vortex, the bound vortex is expected to be smaller.

Figure 18a shows examples of the time history of the lift coefficient for the airfoil at $\alpha = 0^\circ$, $\alpha = 5^\circ$ (pre-stall), and $\alpha = 15^\circ$ (post-stall) for the weak vortex $\Gamma/U_\infty c = 0.55$ and $\varepsilon = 0.6$. The timing of the positive peaks is similar for all cases as it is reached when the vortex arrives to the immediate upstream of the wing. The overall shapes of the time history appear to be shifted vertically for different angles of attack. Figures 18b, c and d present the ratio of the positive lift peaks for the wing and the airfoil at $\alpha = 0^\circ$, $\alpha = 5^\circ$ (pre-stall), and $\alpha = 15^\circ$ (post-stall) as a function of the normalized offset distance for both vortices. The ratio is less than unity for the unloaded wings as well. Again, the aspect ratio correction based on the lifting line theory for steady

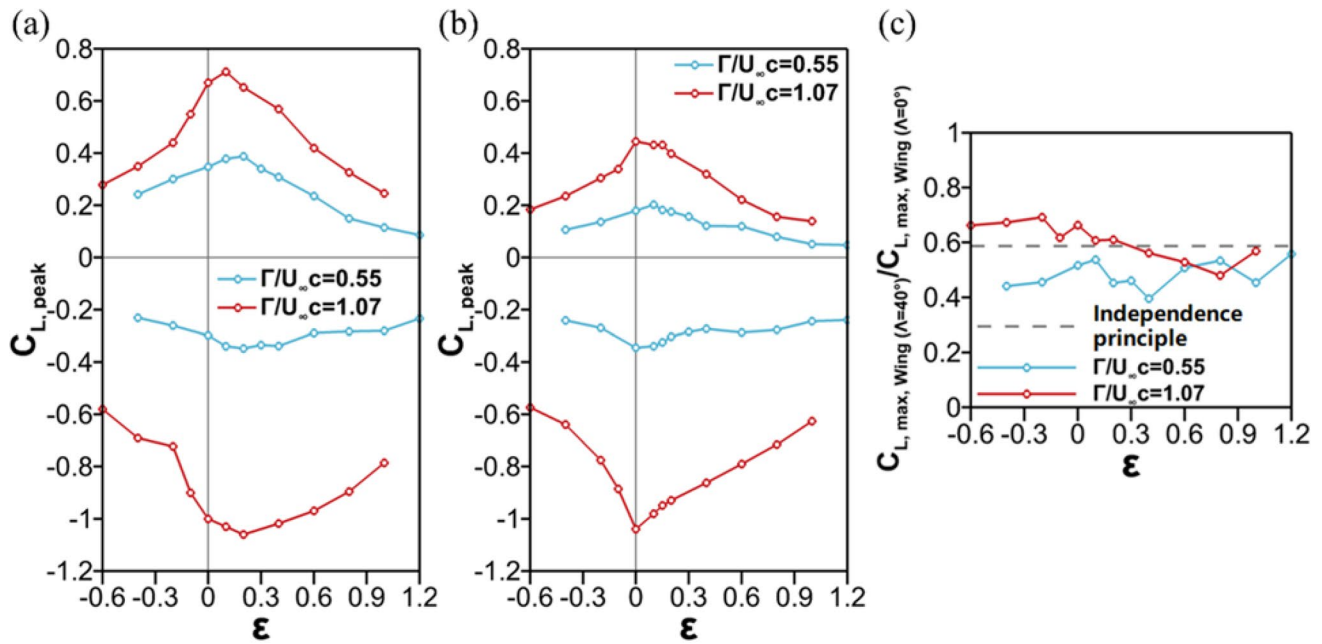


Fig. 15 Peak lift coefficient for **a** unswept wing, and **b** swept wing as a function of offset distance, and **c** the ratio of the peak lift coefficients of the swept wing and unswept wing, $\alpha = 0^\circ$

aerodynamics (shown with the dashed lines) provides a rough estimate for the maximum positive peaks.

It is remarkable that, even for the loaded airfoil (and the unswept wing), the maximum lift induced by the interaction with a single transient vortex can be estimated with the quasi-steady approach. The single transient vortex has large velocity fluctuations that are localized. The temporal gradients are large, but the spatial gradients are confined to a small region. In other words, the length scale of the vortical gust is small, but has large temporal gradients. It will be interesting to make a comparison with plunging airfoils for which the length scale is very large (corresponding to an infinite wavelength of a travelling gust), for which the temporal gradients are felt uniformly everywhere and along the whole chordline. In order to make a comparison with the plunging airfoils in transient motion (Bull et al. 2021), we calculated the ratio of the maximum plunge velocity $V_{p,max}$ to the freestream velocity, and found the equivalent maximum gust angle as:

$$\alpha_{gust,max} = \tan^{-1} (V_{p,max}/U_\infty)$$

The change in the lift coefficient, defined as,

$$\Delta C_{L,max} = C_{L,max} - C_{L,freestream}$$

is plotted in Fig. 19a as a function of $\alpha_{gust,max}$ for the transient plunging airfoil data (Bull et al. 2021, shown with

circles) and our data for the transient travelling vortical gust (shown with triangles). The maximum gust velocity was obtained from the phase-averaged PIV data shown in Fig. 2b. The travelling gusts in the present experiments have large local gust angles but produce much smaller lift increase due to their smaller length-scale.

Another parameter to quantify the unsteadiness is the time rate of the gust velocity. In our case, the dimensionless rate of the gust angle can be defined as:

$$K = \frac{\left(\frac{d\alpha_{gust}}{dt}\right)_{max} c}{2U_\infty}$$

Again, the velocity profiles of the vortices shown in Fig. 2b were used for the calculations. Correspondingly, the parameter K was calculated for the transient plunging motions for the data of Bull et al. (2021). The change of the lift coefficient normalized by the maximum gust angle is shown in Fig. 19b as a function of the non-dimensional rate of the gust angle K . In comparison to the plunging airfoils, the travelling gusts in our experiments have much larger unsteadiness, but much smaller lift change per gust angle regardless of whether the baseline flow is attached or separated. This may be because the effect of the gust (vortex) will not be felt on the whole wing chord. In addition, the maximum positive lift force is reached before the vortex starts to interact closely. This may explain the

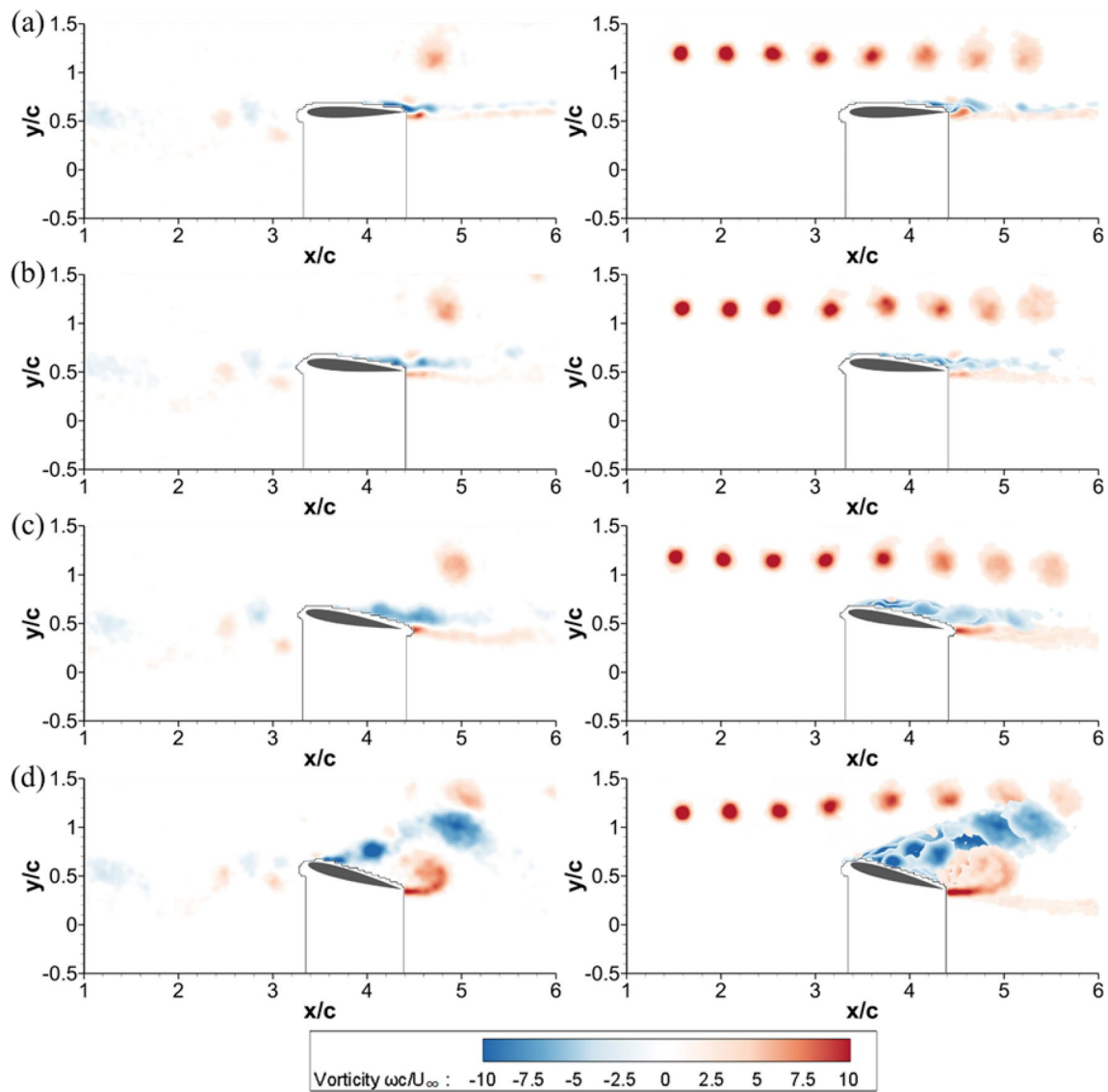


Fig. 16 Vorticity fields at $U_\infty t/c = 5$ (left column) and vortex trajectories (right column) for airfoil interacting with weak vortex $\Gamma/U_\infty c = 0.55$, $\epsilon = 0.6$ for **a** $\alpha = 0^\circ$, **b** $\alpha = 5^\circ$, **c** $\alpha = 10^\circ$, **d** $\alpha = 15^\circ$; data obtained from the PIV measurements

paradoxical result that the maximum positive lift can be estimated with the quasi-steady approach.

3.2.2 Effect of wing sweep

For the loaded wings, the wing sweep could encourage the formation of the leading-edge vortices with spanwise flow during the interaction as the angle of attack is increased. In Fig. 20, the trajectory of the incident vortices is shown by superimposing the vorticity fields at different times for (a) $\alpha = 0^\circ$, (b) $\alpha = 5^\circ$, (c) $\alpha = 15^\circ$ and the strong vortex $\Gamma/U_\infty c = 1.07$, $\epsilon = 0.4$ in the mid-span plane. Intense flow separation and formation of strong leading-edge vortices at nonzero angles of attack are facilitated by the strong incident

vortex in these examples. The nature of the leading-edge vortex filaments and the three-dimensionality of the flow due to the wing sweep are likely to affect the gust response. The isosurfaces of the spanwise vorticity $\omega c/U_\infty = \pm 6, \pm 9, \pm 12$ for the swept wing, superimposed at different times, are shown for the same angles of attack, the same vortex strength and the same offset distance in Fig. 21.

The top views (left column) and the isometric views (right column) in Fig. 21 reveal that as the angle of attack increases, the nature of the leading-edge vortex shedding changes. At zero angle of attack, the leading-edge vortices induced by the incident vortex travels parallel to the incident vortex. (The time history of the phase-averaged flow is shown in Fig. 12 at different times for this case). In contrast,

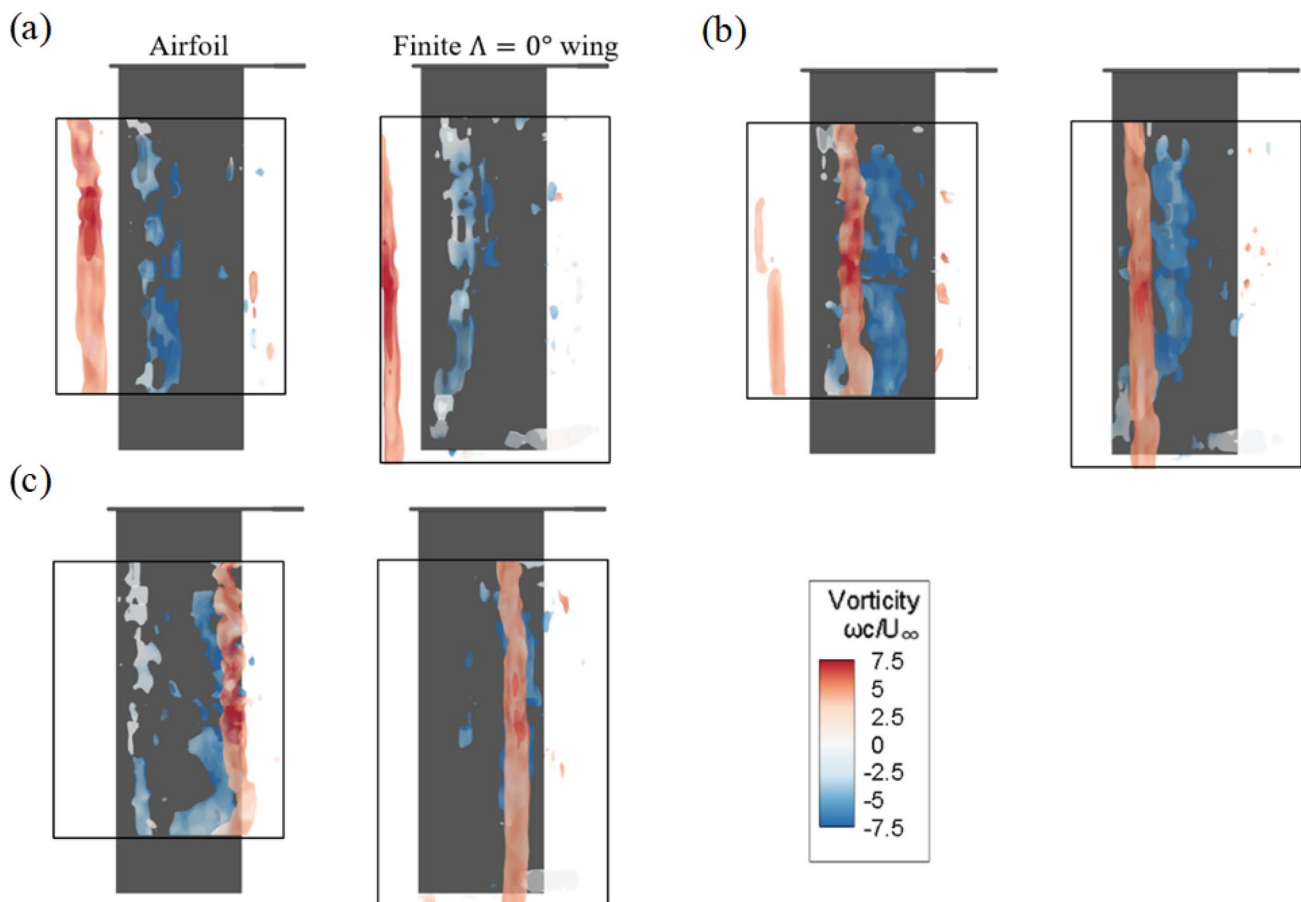


Fig. 17 Comparison of iso-surfaces of $Q^* = 5, 35, 50, 70$, coloured by spanwise vorticity, at **a** $U_\infty t/c = 3.5$, **b** $U_\infty t/c = 4$, **c** $U_\infty t/c = 4.5$, for the airfoil (left) and the wing (right) and weak vortex $\Gamma/U_\infty c = 0.55$, $\varepsilon = 0.6$, $\alpha = 10^\circ$; data obtained from the volumetric velocity measurements

for the post-stall angle of attack of $\alpha = 15^\circ$, the leading-edge vortices appear to develop parallel to the leading-edge. For $\alpha = 5^\circ$, it is likely to be a mix of the two modes. For all cases, the incident vortex remains nearly-two-dimensional before the interaction with the wing. However, the inboard part of the incident vortex is highly diffused and weakened for all three angles of attack. For the largest angle of attack, the isometric view of the incident vortex reveals the substantial deformation and deflection downwards.

Figure 22 presents the time history of the lift coefficient for varying offset distances at (a) $\alpha = 0^\circ$, (b) $\alpha = 5^\circ$ (pre-stall), and (c) $\alpha = 15^\circ$ (post-stall) for the strong vortex. In all cases, the shape of the lift history looks similar. The timings of the positive and negative peaks are the same for all cases and angles of attack. The difference between the positive peak and the negative peak (peak-to-peak amplitude of the lift) decreases with increasing angle of attack. This is presumably due to the decreasing flow separation on the lower surface and attenuated negative lift, which is normally dominated by the viscous effects.

The peak lift coefficients corresponding to the maximum and minimum values in the time history are shown in Fig. 23 as a function of the normalized offset distance for both the strong and weak incident vortex. Here, the dashed lines show the corresponding lift coefficient in freestream at each angle of attack. The peak-to-peak amplitude is maximum near the zero offset distance and decreases with increasing angle of attack. For the largest angle of attack, the minimum lift coefficient is positive for the weak vortex, but only positive for the strong vortex when the vortex is far away from the wing. These are indications of decreasing viscous effects on the lower surface of the wing. Focusing on the positive peaks for which the inviscid mechanism is believed to be dominant, they are roughly symmetric with the offset distance for small angle of attack, but become clearly asymmetric for the largest angle of attack. In this case, the decay of the positive lift coefficient with ε is different for positive and negative offset distances. It appears that, for positive offset distances, there is always larger peaks than for the negative offset distances.

This is illustrated in Fig. 24 by plotting the ratio of the positive peak lift coefficients of the swept wing and the

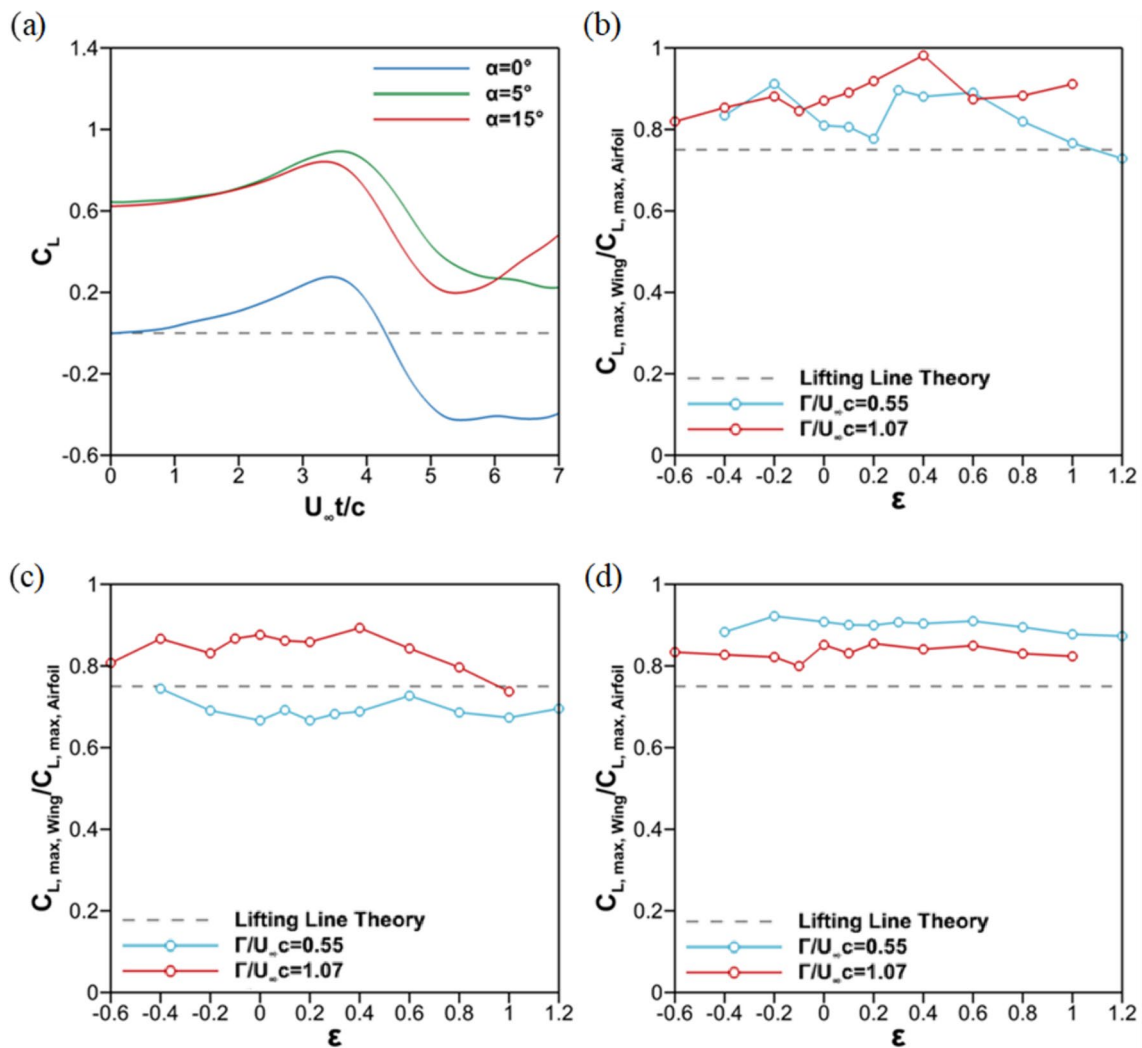


Fig. 18 **a** Comparison of lift time history for airfoil with weak vortex $\Gamma/U_\infty c = 0.55$, $\epsilon = 0.6$ at various α ; the ratio of the positive lift peaks of the wing and the airfoil for **b** $\alpha = 0^\circ$, **c** $\alpha = 5^\circ$, **d** $\alpha = 15^\circ$

unswept wing. Again, the dashed lines correspond to the “independence principle”. For small angles of attack, the measured ratio is not too far away from that of the independence principle. In contrast, there is increased lift for the unswept wing at the largest angle of attack for all offset distances. We think that the induced upwash of the counter-clockwise vortex as it approaches the wing produces leading-edge vortex on the upper surface of the swept wing. This results in larger peak lift than the estimate of the independence principle.

The vortex-wing interaction for the swept wing at $\alpha = 15^\circ$ was investigated further using the PIV and volumetric 3-component velocity measurements for the strong vortex $\Gamma/U_\infty c = 1.07$ and $\epsilon = 0.4$. Figure 25 presents the iso-surfaces of the spanwise vorticity obtained from the PIV measurements in multiple spanwise planes. We note that for this angle of attack, the flow is already separated near the

leading-edge in the absence of the incident vortex. Consequently, there is already flow separation near the leading-edge at $U_\infty t/c = 2$ when the incident vortex is upstream of the wing. This is in contrast with the case of $\alpha = 0^\circ$ shown in Fig. 12 for the same vortex strength and offset distance. In Fig. 25, as the incident vortex moves over the wing there is always flow separation from the leading-edge downstream of the incident vortex (outboard sections of the wing). However, upstream of the incident vortex (inboard sections of the wing), flow separation is not visible, which is due to the downwash of the incident vortex. The spanwise extent of the flow separation at the leading-edge, confined between the leading-edge section just below the incident vortex and the wing-tip, shrinks as the incident vortex travels over the wing. Even at the last instant shown $U_\infty t/c = 5.5$, there is still no flow separation established behind the incident vortex, indicating that its downwash still suppresses the flow separation.

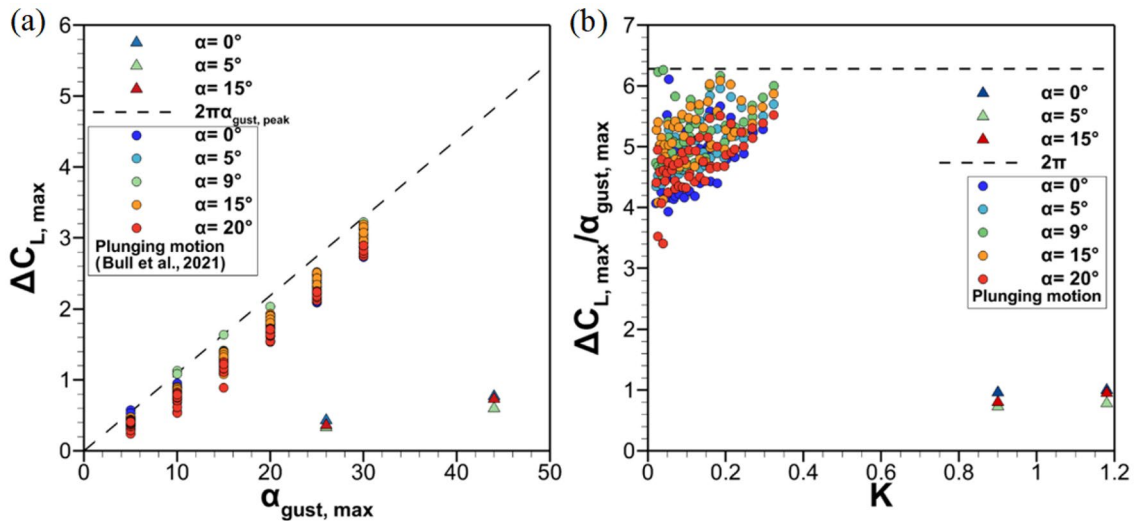


Fig. 19 Variation of **a** lift coefficient increase with maximum gust angle, and **b** change of lift coefficient normalized by the maximum gust angle as a function of non-dimensional rate of gust angle K

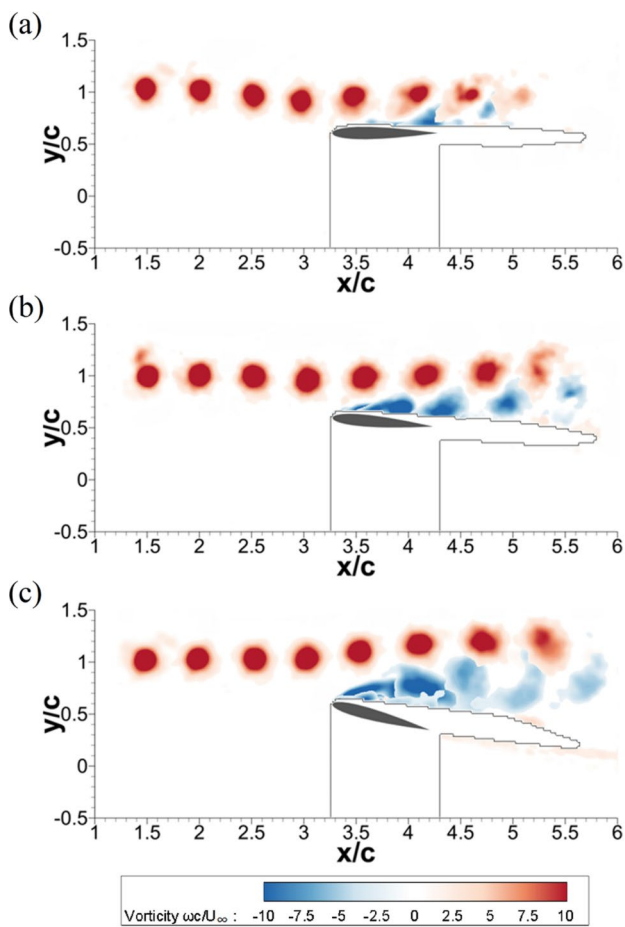


Fig. 20 Vortex trajectory at the midspan plane of the swept wing for various angles of attack **a** $\alpha = 0^\circ$, **b** $\alpha = 5^\circ$, **c** $\alpha = 15^\circ$; strong vortex $\Gamma/U_\infty c = 1.07$, $\epsilon = 0.4$

It is also noticed in Fig. 25 that a second region of vorticity downstream of the incident vortex starts to develop from near the root. Unlike the first stationary vorticity region near the leading-edge, the second region of vorticity travels with the incident vortex while remaining always downstream of the incident vortex over the outboard sections of the wing. The iso-surfaces of Q^* shown in Fig. 26 between $U_\infty t/c = 3$ and 4.5 confirm that the region of vorticity moving with the incident vortex is a leading-edge vortex. In contrast, the stationary region of vorticity near the leading-edge observed in Fig. 25 does not appear in the Q -surfaces, confirming that this region corresponds to the separated shear layer, but is not a “leading-edge vortex”. The isosurfaces of Q^* in Fig. 26 are coloured by the spanwise velocity w/U_∞ and w'/U_∞ . Here, w/U_∞ is the spanwise velocity in the incident vortex along the z -spanwise axis and w'/U_∞ is the spanwise velocity along the axis parallel to the leading-edge of the wing. For both definitions of the spanwise velocity, the positive velocity is in the outboard direction. There is negligible spanwise flow in the incident vortex upstream of the wing and during the interaction with the wing. In contrast, there is strong spanwise flow in the leading-edge vortex, especially in the inboard parts of the vortex filament. The outboard parts of the vortex filament exhibit characteristics of vortex breakdown. The angle between the axis of the leading-edge vortex at $U_\infty t/c = 3$ and the freestream direction is slightly larger than the wing sweep angle. The leading-edge vortex is nearly parallel to the wing leading-edge at $U_\infty t/c = 3.5$ and 4.0, but later in the wake becomes nearly parallel to the incident vortex. It is clear that the leading-edge vortex sheds and travels downstream. In other words, we do not observe a stationary

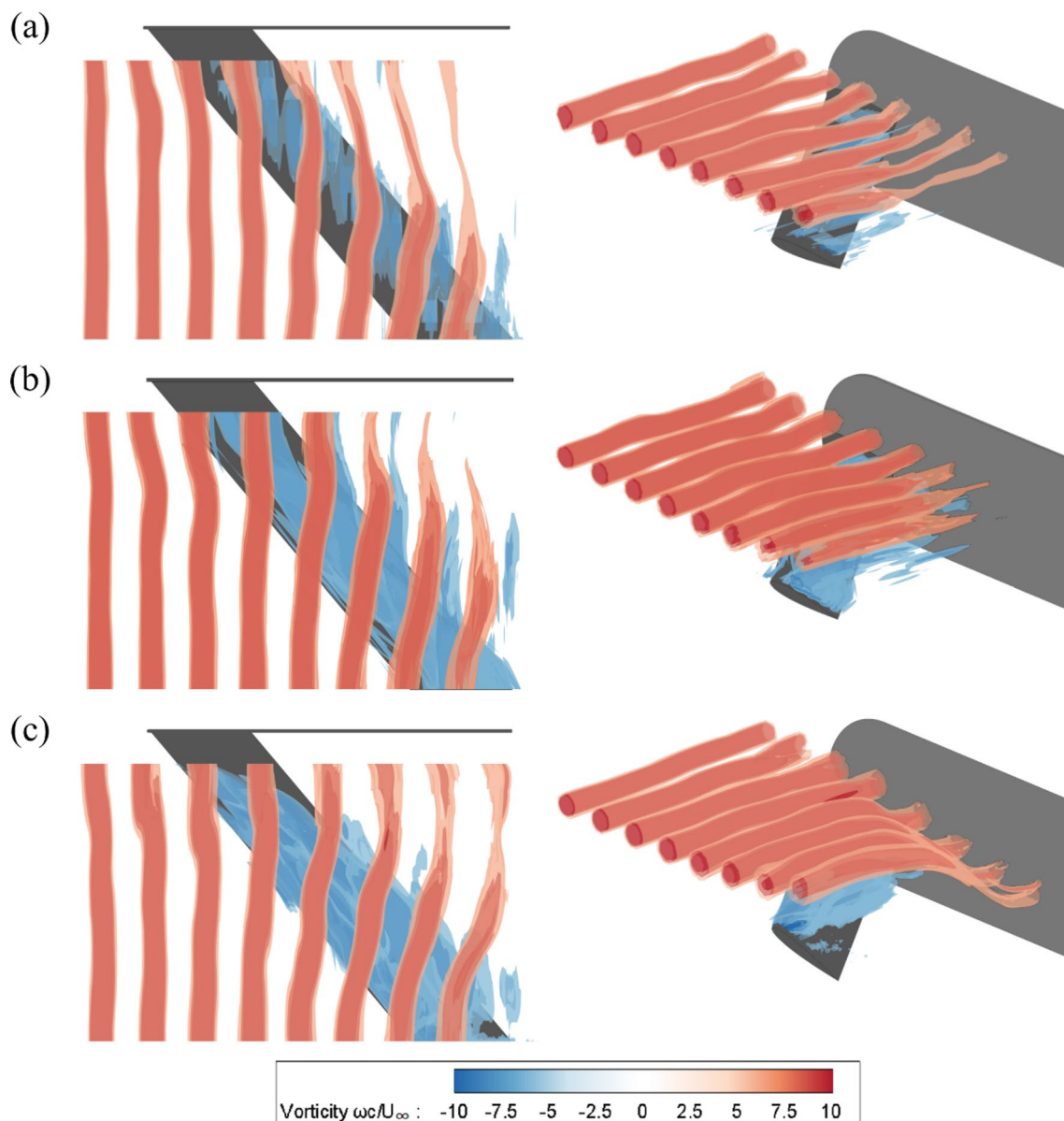


Fig. 21 Iso-surfaces of the spanwise vorticity $\omega c/U_\infty = \pm 6, \pm 9, \pm 12$ for the swept wing, superimposed at different times, for **a** $\alpha = 0^\circ$, **b** $\alpha = 5^\circ$, **c** $\alpha = 15^\circ$; strong vortex $\Gamma/U_\infty c = 1.07$, $\varepsilon = 0.4$. Top view (left column) and isometric view (right column)

leading-edge vortex attached to the wing surface, at least for this sweep angle, as we would for traditional delta wing vortices. Such vortices can remain attached to the wing during an unsteady motion.

4 Conclusions

The interaction of a nearly two-dimensional vortical gust with airfoils, finite unswept and swept wings was investigated in a water tunnel investigation. A single vortex was produced by plunging an upstream airfoil fast and then

bringing it to a complete stop slowly. This transient plunge motion effectively generated a single counter-clockwise vortex during the high plunge velocity phase, which travelled with a convection speed that is approximately equal to the freestream velocity. In contrast, the vorticity layer of the opposite sign shed from the upstream airfoil did not roll up during the slow plunge velocity phase. The phase-averaged PIV as well as volumetric three-component velocity measurements confirmed that the vortical gust is nearly uniform in the spanwise direction. The offset distance of the vortex center from the airfoil/wing leading-edge in the cross-stream direction as well as the angle of attack of the airfoil/wing

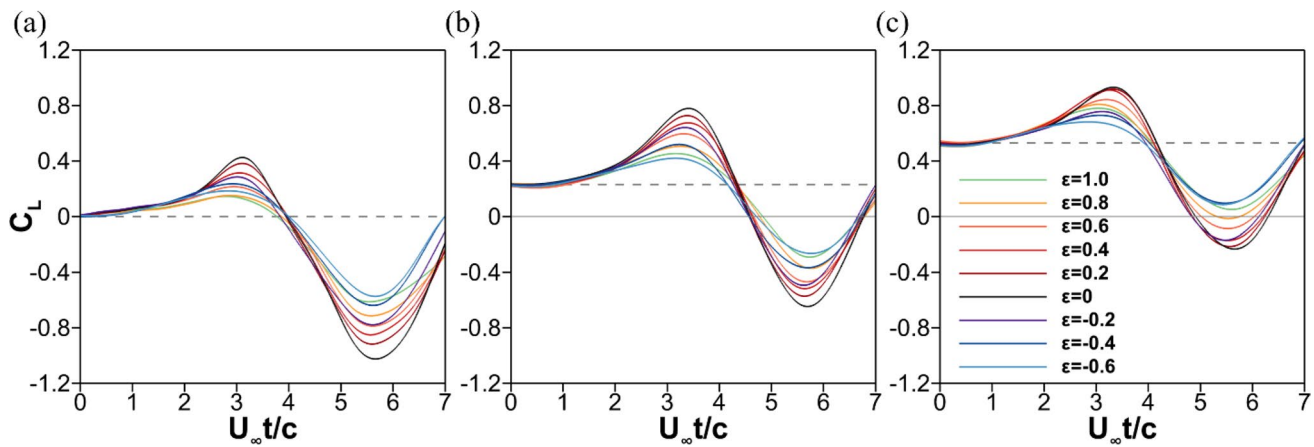


Fig. 22 Time history of lift coefficient for the swept $\Lambda = 40^\circ$ wing at various angles of attack **a** $\alpha = 0^\circ$, **b** $\alpha = 5^\circ$, **c** $\alpha = 15^\circ$; strong vortex $\Gamma/U_\infty c = 1.07$.

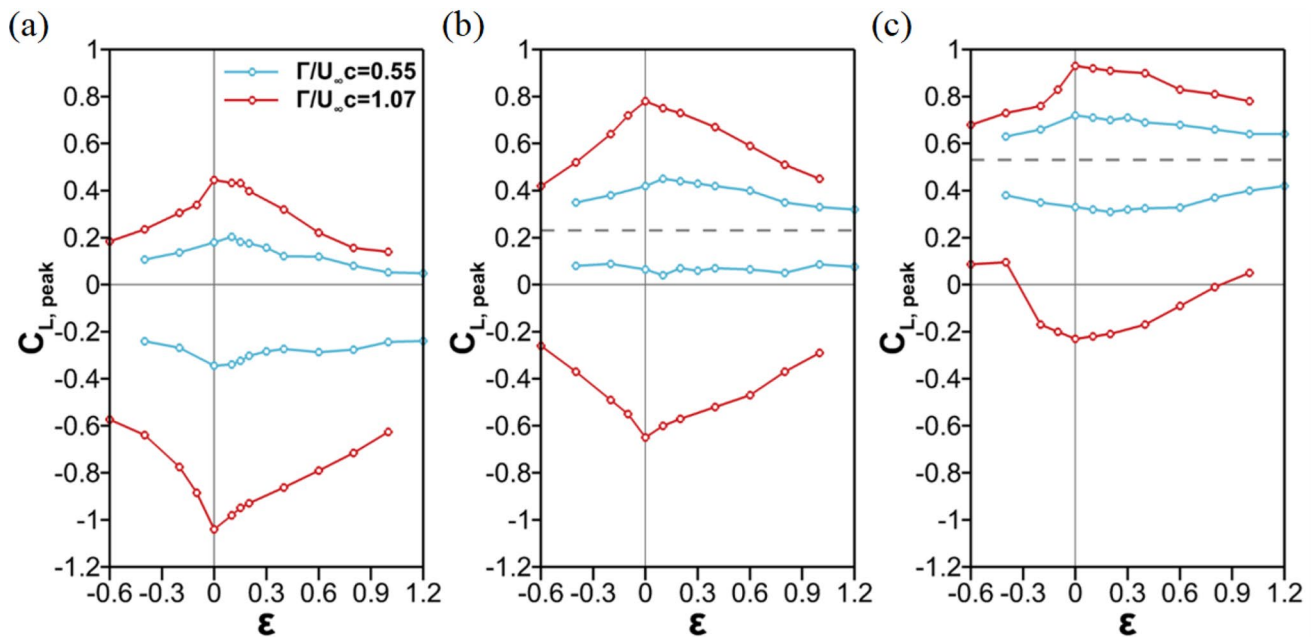


Fig. 23 Peak lift coefficients for the swept $\Lambda = 40^\circ$ wing as a function of the normalized offset distance at various angles of attack **a** $\alpha = 0^\circ$, **b** $\alpha = 5^\circ$, **c** $\alpha = 15^\circ$ for both incident vortices

were varied. The interaction of the incident vortex with the wing, the turbulent diffusion of the incident vortex, generation of the leading-edge vortices from the wing, the spanwise flow in the incident vortex and the leading-edge vortex, and the scaling of the peak lift coefficients for the airfoil, unswept wing and the swept wing were discussed.

For unloaded airfoils and wings (set at zero angle of attack), flow separation from the leading-edge is not noticeable as the vortex approaches. There might be weak flow separation if it is a close interaction. Generally, there is turbulent diffusion of the incident vortex as the interaction

becomes closer and stronger. The turbulent diffusion becomes faster as the vortex leaves the trailing-edge and moves onto the wake. It is suggested that other vortices, flow separation and wake produce disturbances and may cause instabilities in the incident spanwise vortex. There is no evidence of significant spanwise flow developing in the incident vortices, even for the interaction with the swept wing. The measurements show that the turbulent diffusion remains limited to the sections of the spanwise vortex that already interacted with the swept wing.

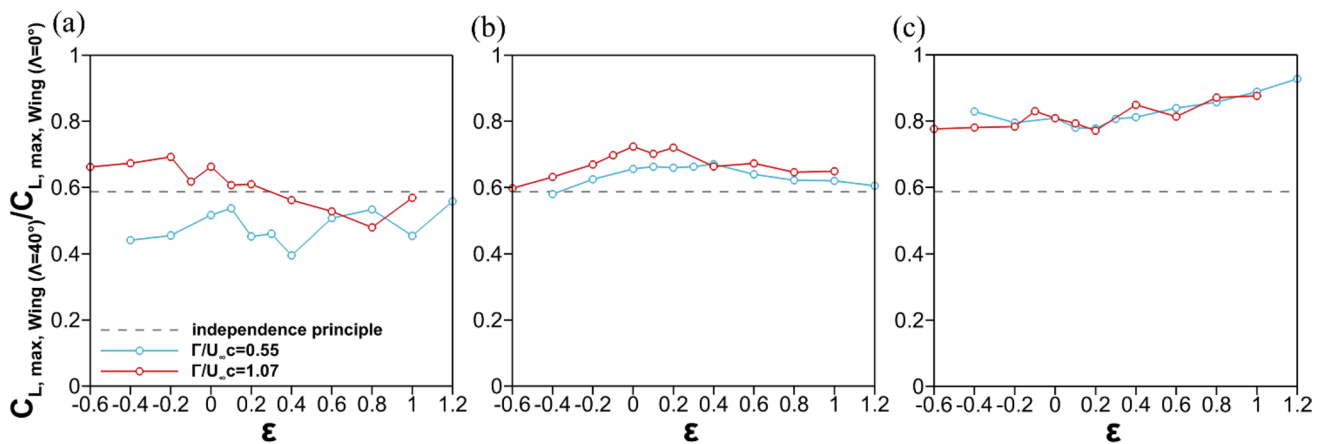


Fig. 24 Ratio of the positive peak lift coefficients of the swept and unswept wing as a function of the normalized offset distance for **a** $\alpha = 0^\circ$, **b** $\alpha = 5^\circ$, **c** $\alpha = 15^\circ$

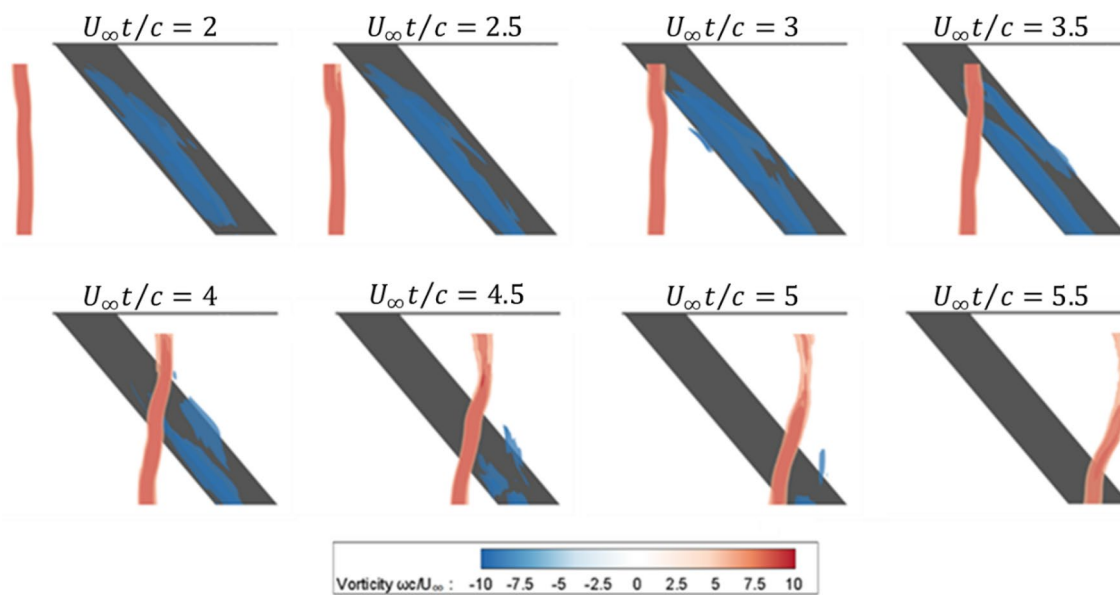


Fig. 25 Iso-surfaces of spanwise vorticity $\omega c/U_\infty = 6, \pm 9, \pm 12$ at different times for the strong vortex $\Gamma/U_\infty c = 1.07$, $\epsilon = 0.4$, $\alpha = 15^\circ$; data obtained from the PIV measurements

As the counter-clockwise vortex approaches the airfoil or wing, it generates a positive peak lift. The positive peak occurs when the vortex is roughly five vortex core radius from the leading-edge. At this instant, there is no evidence of flow separation from the leading-edge even for the zero offset case. We suggest that the positive peak is inviscid in nature. A simple reduced order model based on the lumped vortex model can predict the qualitative variation of the unsteady lift history and the magnitude of the positive peak. Furthermore, by assuming that the quasi-steady lift is dominant, we are able to predict that the peak lift force is proportional to the circulation of the incident vortex and has a

maximum for the zero offset distance. These predictions are in reasonable agreement with our data. Unlike the positive peak, the negative lift is generated as the incident vortex has passed the wing and continues to produce downwash on the wing. The duration of the negative lift is relatively longer. The viscous effects become important as the flow separation on the lower surface of the wing occurs. The reduced order model, which is inviscid in nature, is less successful for the negative peak lift. The time history of the lift for the airfoil and the unswept wing are similar, including the timing of the peak lift coefficients. However, the maximum lift of the wing is smaller due to the downwash of the finite wing. The

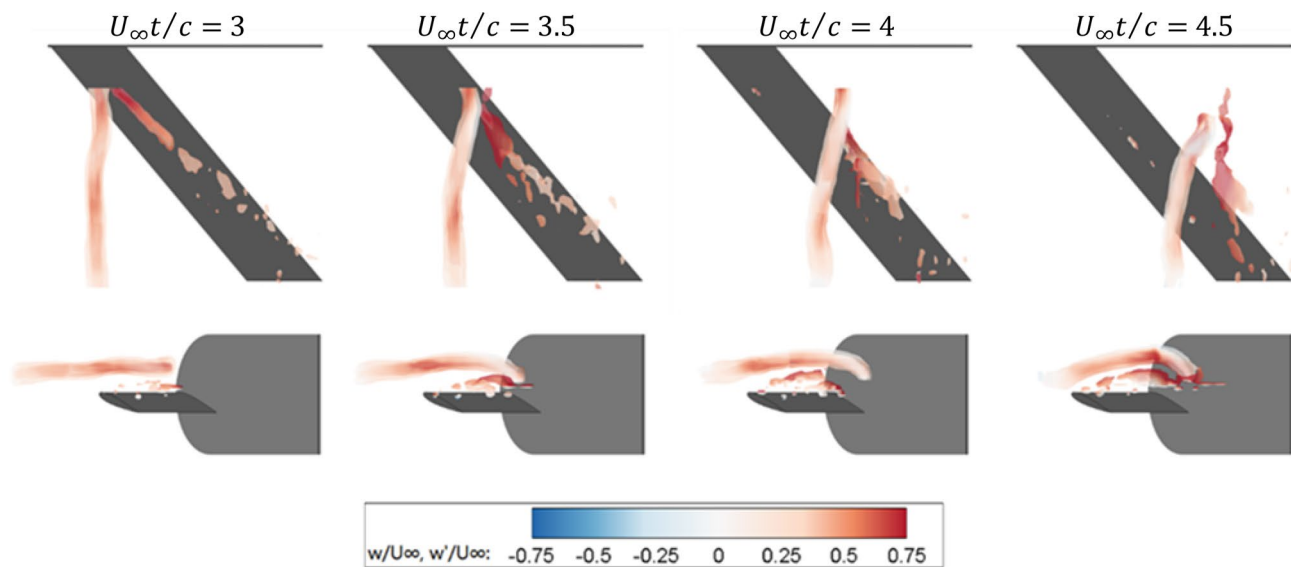


Fig. 26 Isosurfaces of $Q^* = 5, 35, 50, 70$, coloured by spanwise velocity w/U_∞ and w'/U_∞ , obtained from the volumetric measurements, for the strong vortex $\Gamma/U_\infty c = 1.07$, $\varepsilon = 0.4$, $\alpha = 15^\circ$

positive lift peak can be estimated by using an aspect ratio correction developed for steady aerodynamics, which supports the hypothesis of the quasi-steady interaction.

The interaction with the swept wing at each spanwise plane appears unaffected by the other spanwise planes. As a result, the strip-theory approach for the swept wing captures the main features of the unsteady lift. The decrease of the peak lift and the temporal gradients for the swept wing is the main feature of the observations. Interestingly, the positive peak lift can be estimated by using the independence principle, which was developed for steady aerodynamics.

For the loaded airfoil and unswept wing, flow separation and formation of a leading-edge vortex become more pronounced with increasing angle of attack. Yet, the positive peak lift force is attained before the vortex starts to interact with the wing, similarly to the unloaded airfoils and wings. Again, the aspect ratio correction based on the lifting line theory for steady aerodynamics provides a rough estimate for the maximum positive peaks. Overall, the incident vortices generated in the present experiments produce large velocity fluctuations but cause small lift changes due to their small length-scale compared to the wing chord line.

For the loaded swept wing, as the angle of attack increases, the nature of the leading-edge vortex shedding changes. The shedding of the leading-edge vortices is parallel to the incident vortex at small incidences. In contrast, the shedding becomes parallel to the leading-edge of the wing at the post-stall angle of attack. As the incident counter-clockwise vortex approaches the wing, it induces upwash. The separated shear layer rolls up into leading-edge vortex, which travels with the incident vortex while

always remaining downstream of the incident vortex. There is also evidence of significant spanwise flow developing in the leading-edge vortex. A stationary leading-edge vortex attached to the wing surface is not observed, at least for this sweep angle. Nevertheless, the parallel shedding process of the leading-edge vortex over the wing results in larger peak lift force than predicted by the independence principle.

Acknowledgements The authors would like to acknowledge the Engineering and Physical Sciences Research Council (EPSRC) strategic equipment Grant No. EP/K040391/1.

Data availability The data that support the findings of this study are available from the corresponding author upon reasonable request.

Open Access This article is licensed under a Creative Commons Attribution 4.0 International License, which permits use, sharing, adaptation, distribution and reproduction in any medium or format, as long as you give appropriate credit to the original author(s) and the source, provide a link to the Creative Commons licence, and indicate if changes were made. The images or other third party material in this article are included in the article's Creative Commons licence, unless indicated otherwise in a credit line to the material. If material is not included in the article's Creative Commons licence and your intended use is not permitted by statutory regulation or exceeds the permitted use, you will need to obtain permission directly from the copyright holder. To view a copy of this licence, visit <http://creativecommons.org/licenses/by/4.0/>.

References

- Antkowiak A, Brancher P (2004) Transient energy growth for the Lamb-Oseen vortex. *Phys Fluids* 16(1):L1–L4

- Barnes CJ, Visbal MR (2018a) Counterclockwise vortical-gust/airfoil interactions at a transitional Reynolds number. *AIAA J* 56(7):2540–2552
- Barnes CJ, Visbal MR (2018b) Clockwise vortical-gust/airfoil interactions at a transitional Reynolds number. *AIAA J* 56(10):3863–3874
- Barnes CJ, Visbal MR (2019) Computational investigation of the effect of sweep on parallel vortical-gust/wing interactions. In *AIAA Scitech 2019 Forum* (AIAA 2019–0896)
- Barnes CJ, Visbal MR (2020) Angle of attack and core size effects on transitional vortical-gust–airfoil interactions. *AIAA J* 58(7):2881–2898
- Bicknell J, Parker A (1972) A wind-tunnel stream oscillation apparatus. *J Aircr* 9(6):446–447
- Bölle T, Brion V, Robinet JC, Sipp D, Jacquin L (2021) On the linear receptivity of trailing vortices. *J Fluid Mech* 908:A8
- Booth ER Jr, Yu JC (1986) Two-dimensional blade-vortex flow visualization investigation. *AIAA J* 24(9):1468–1473
- Brion V, Lepage A, Amosse Y, Soulevant D, Senecat P, Abart JC, Paillart P (2015) Generation of vertical gusts in a transonic wind tunnel. *Exp Fluids* 56(7):1–16
- Bull S, Chiereghin N, Cleaver DJ, Gursul I (2020) Novel approach to leading-edge vortex suppression. *AIAA J* 58(10):4212–4227
- Bull S, Chiereghin N, Gursul I, Cleaver DJ (2021) Unsteady aerodynamics of a plunging airfoil in transient motion. *J Fluids Struct* 103:103288
- Calderon DE, Wang Z, Gursul I, Visbal MR (2013a) Volumetric measurements and simulations of the vortex structures generated by low aspect ratio plunging wings. *Phy Fluids* 25(6):067102
- Calderon DE, Wang Z, Gursul I (2013b) Lift-enhancing vortex flows generated by plunging rectangular wings with small amplitude. *AIAA J* 51(12):2953–2964
- Chen H, Jaworski JW (2020) Aeroelastic interactions and trajectory selection of vortex gusts impinging upon Joukowski airfoils. *J Fluids Struct* 96:103026
- Chiereghin N, Cleaver DJ, Gursul I (2019) Unsteady lift and moment of a periodically plunging airfoil. *AIAA J* 57(1):208–222
- Chiereghin N, Bull S, Cleaver DJ, Gursul I (2020) Three-dimensionality of leading-edge vortices on high aspect ratio plunging wings. *Phys Rev Fluids* 5(6):064701
- Cleaver DJ, Wang Z, Gursul I, Visbal MR (2011) Lift enhancement by means of small-amplitude airfoil oscillations at low Reynolds numbers. *AIAA J* 49(9):2018–2033
- Cleaver D, Wang Z, Gursul I (2012) Bifurcating flows of plunging aerofoils at high Strouhal numbers. *J Fluid Mech* 708:349–376
- Cleaver DJ, Wang Z, Gursul I (2013) Investigation of high-lift mechanisms for a flat-plate airfoil undergoing small-amplitude plunging oscillations. *AIAA J* 51(4):968–980
- Doligalski TL, Smith CR, Walker JDA (1994) Vortex interactions with walls. *Annu Rev Fluid Mech* 26(1):573–616
- Eloy C, Le Dizès S (1999) Three-dimensional instability of Burgers and Lamb–Oseen vortices in a strain field. *J Fluid Mech* 378:145–166
- Gilman J Jr, Bennett RM (1966) A wind-tunnel technique for measuring frequency-response functions for gust load analyses. *J Aircr* 3(6):535–540
- Gursul I, Cleaver D (2019) Plunging oscillations of airfoils and wings: Progress, opportunities, and challenges. *AIAA J* 57(9):3648–3665
- Gursul I, Rockwell D (1990) Vortex street impinging upon an elliptical leading edge. *J Fluid Mech* 211:211–242
- Heathcote SF (2006) Flexible flapping airfoil propulsion at low Reynolds numbers. PhD Dissertation, University of Bath
- Jones AR, Cetiner O, Smith MJ (2022) Physics and modeling of large flow disturbances: discrete gust Encounters for modern air vehicles. *Annu Rev Fluid Mech* 54:469–493
- Jones WP, Moore JA (1972) Flow in the wake of a cascade of oscillating airfoils. *AIAA J* 10(12):1600–1605
- Katz J, Plotkin A (2001) *Low-speed aerodynamics* (2nd edn, Cambridge Aerospace Series). Cambridge University Press, Cambridge, pp 381–385
- Kaykayoglu R, Rockwell D (1985) Vortices incident upon a leading edge: instantaneous pressure fields. *J Fluid Mech* 156:439–461
- Kuethe AM, Chow CY, Fung YC (1998) Bases of aerodynamics design. In: *Foundations of aerodynamics*, 5th ed. John Wiley & Sons, New York, pp 337–339
- Martínez-Muriel C, Flores O (2020) Analysis of vortical gust impact on airfoils at low Reynolds number. *J Fluids Struct* 99:103138
- Moffat RJ (1988) Describing the uncertainties in experimental results. *Exp Therm Fluid Sci* 1(1):3–17
- Panaras AG (1987) Numerical modeling of the vortex/airfoil interaction. *AIAA J* 25(1):5–11
- Peng D, Gregory JW (2015) Vortex dynamics during blade-vortex interactions. *Phys Fluids* 27(5):053104
- Peng D, Gregory JW (2017) Asymmetric distributions in pressure/load fluctuation levels during blade-vortex interactions. *J Fluids Struct* 68:58–71
- Pradeep DS, Hussain F (2006) Transient growth of perturbations in a vortex column. *J Fluid Mech* 550:251–288
- Qian Y (2022) Interaction of vortical gusts with wings. PhD Dissertation (to be submitted), University of Bath
- Rockwell D (1998) Vortex-body interactions. *Annu Rev Fluid Mech* 30(1):199–229
- Rockwell D, Knisely C (1979) The organized nature of flow impingement upon a corner. *J Fluid Mech* 93(3):413–432
- Son O, Gao AK, Gursul I, Cantwell CD, Wang Z, Sherwin S (2022) Leading-edge vortex dynamics on plunging airfoils and wings. *J Fluid Mech* 940:A28
- Tsai CY, Widnall SE (1976) The stability of short waves on a straight vortex filament in a weak externally imposed strain field. *J Fluid Mech* 73(4):721–733
- Turhan B, Wang Z, Gursul I (2022) Coherence of unsteady wake of periodically plunging airfoil. *J Fluid Mech* 938:A14
- Waleffe F (1990) On the three-dimensional instability of strained vortices. *Phys Fluids a: Fluid Dyn* 2(1):76–80
- Wei NJ, Kissing J, Tropea C (2019a) Generation of periodic gusts with a pitching and plunging airfoil. *Exp Fluids* 60(11):166
- Wei NJ, Kissing J, Wester TT, Wegt S, Schiffmann K, Jakirlic S, Holling M, Peinke J, Tropea C (2019b) Insights into the periodic gust response of airfoils. *J Fluid Mech* 876:237–263
- Wilder MC, Telionis DP (1998) Parallel blade–vortex interaction. *J Fluids Struct* 12(7):801–838
- Wu Z, Bangga G, Lutz T, Kampers G, Hölling M (2020) Insights into airfoil response to sinusoidal gusty inflow by oscillating vanes. *Phys Fluids* 32(12):125107
- Ziada S, Rockwell D (1982) Vortex–leading-edge interaction. *J Fluid Mech* 118:79–107